

Hybrid Beamforming for Active Sensing using Sparse Arrays

Robin Rajamäki[†], *Student Member, IEEE*, Sundeep Prabhakar
Chepuri^{*}, *Member, IEEE*, and Visa Koivunen[†], *Fellow, IEEE*

Abstract

This paper studies hybrid beamforming for active sensing applications, such as millimeter-wave or ultrasound imaging. Hybrid beamforming can substantially lower the cost and power consumption of fully digital sensor arrays by reducing the number of active front ends. Sparse arrays can be used to further reduce hardware costs. We consider phased arrays and employ linear beamforming with possibly sparse array configurations at both the transmitter and receiver. The quality of the acquired images is improved by adding together several component images corresponding to different transmissions and receptions. In order to limit the acquisition time of an image, we formulate an optimization problem for minimizing the number of component images subject to achieving a desired point spread function. Since this problem is not convex, we propose algorithms for finding approximate solutions in the fully digital beamforming case, as well as in the more challenging hybrid and analog beamforming cases that employ quantized phase shifters. We also determine upper bounds on the number of component images needed for achieving the fully digital solution using fully analog and hybrid architectures, and derive closed-form expressions for the beamforming weights in these cases. Simulations demonstrate that a hybrid sparse array with very few elements, and even fewer front ends, can achieve the resolution of a fully digital uniform array at the expense of a longer image acquisition time.

Index Terms

Active sensing, hybrid beamforming, image addition, phased array, sparse arrays, sum co-array.

[†]Department of Signal Processing and Acoustics, Aalto University, Espoo, Finland. (e-mail: robin.rajamaki@aalto.fi, visa.koivunen@aalto.fi)

^{*}Department of Electrical Communication Engineering, Indian Institute of Science, Bangalore, India (e-mail: spchehuri@iisc.ac.in).

This work was supported in part by the Academy of Finland project “Massive and Sparse Antenna Array Processing for Millimeter-Wave Communications”, and the Tata Trusts.

I. INTRODUCTION

Sensor arrays are a key technology with several applications in radar, sonar, microwave imaging, medical ultrasound, and wireless communications, to list a few [1]. The many advantages of arrays include high signal-to-noise ratio (SNR) gain, spatial diversity, and the capability to cancel interferences by beamforming. The ability to resolve targets improves with increasing aperture, which encourages using short carrier wavelengths. This allows for designing electrically large arrays with small form factors by packing a very large number (on the order of hundreds) of elements into a tiny (on the order of a cm^2) physical area. On the other hand, the cost, power consumption, and computational load commonly associated with signal processing for many antenna elements and dedicated transceiver chains may become prohibitively large. These issues are especially pronounced for fully digital arrays, where each array element is connected to separate *front end*, which includes *radio* and *intermediate frequency* (RF-IF) components and an *analog-to-digital converter* (ADC) or a *digital-to-analog converter* (DAC). For example, a planar antenna array operating in the THz frequencies of the radio spectrum may in principle even fit thousands of elements in an area of only a few square centimeters. The practical applicability of such fully digital systems is limited by the number of required RF-IF front ends, and the typical high sampling rates and bandwidths imposed on the DACs/ADCs.

Sparse arrays can be used to reduce the cost of large arrays with a regular geometry. By utilizing a virtual array model called the *co-array*, the number of elements can be significantly reduced compared to a uniform array of equivalent aperture, without sacrificing the array's ability to resolve scatterers or signal sources [2]–[4]. The co-array is a virtual array structure typically consisting of the pairwise vector sums or differences of the physical array element positions. For instance, the *sum co-array* commonly arises in active sensing applications, where linear processing (delay-and-sum beamforming and matched filtering) is used at the transmitter and receiver. Sparse arrays exploit the fact that the co-array of a uniform array is redundant. Redundancy implies that the same co-array can be achieved using fewer physical elements by carefully placing the sensors in a sparse manner.

The support of the co-array ultimately determines the achievable set of *point spread functions* (PSFs), which determine the properties of the imaging system. A particular PSF may be achieved by weighting the co-array using the so-called *image addition* technique [2]. Image addition produces a desired co-array weighting by adding together several images, which are acquired using

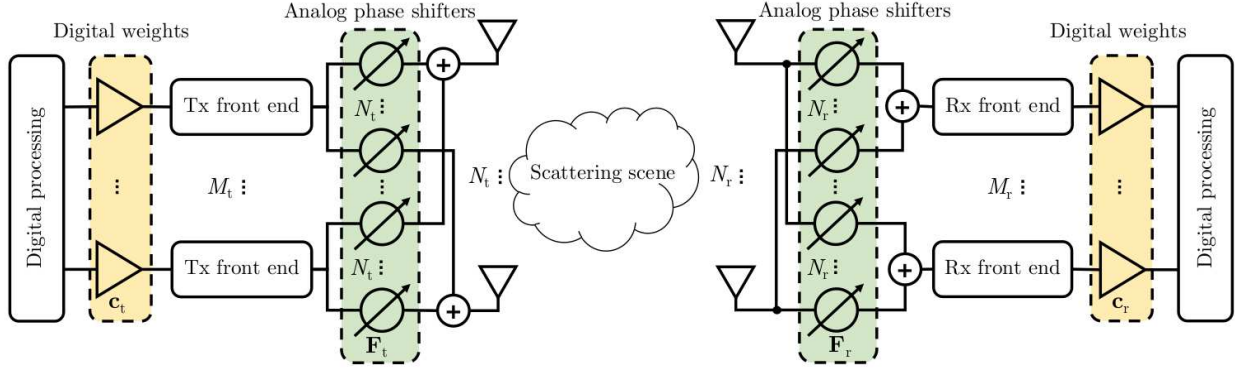


Fig. 1: Fully connected hybrid beamforming architecture of transmitter and receiver. Each digital weight (element of vector \mathbf{c}_x) and array element is connected via a front end and a phase shifter with discretized phase (element of matrix \mathbf{F}_x).

different transmit-receive beamforming weights. Each of these component weights correspond to a separate transmission, or pulse, and reception, when transmitters operate coherently as in a phased array. In this case, it is critical to keep the number of component images as low as possible to reduce the image acquisition time, while controlling the distortions to the PSF. If transmissions are incoherent, as in synthetic aperture radar, or orthogonal multiple-input-multiple-output (MIMO) radar [5], the number of component images is less important. In such cases, image addition may be applied during post-processing after data acquisition [6].

Hybrid beamforming may be used to further lower the cost of a fully digital array. Hybrid beamforming architectures reduce the number of front ends by pre-processing the transmitted or received signals by an analog beamforming network. This network usually consists of inexpensive, low power phase shifters connecting every array element to all front ends. Fig. 1 depicts this *fully connected* architecture. In a partially connected architecture, each front end is connected to only a subset of all the available elements [7]. The total power consumption and cost of the system may further be reduced by applying coarser quantization at the ADCs/DACs [8], [9], or by using sparse arrays. The typical application of hybrid beamforming is *millimeter-wave* (mmWave) communications, where linear processing is used to precode and decode multiple data streams sent over a MIMO channel, with the goal of maximizing the spectral efficiency [9] or minimizing the mean squared error of the received data [10].

The design of the hybrid beamformer is challenging as it requires solving a non-convex optimization problem. In particular, non-convexity results from i) decomposing the fully digital

beamformer into analog and digital parts; ii) introducing phase shifters in the analog beamforming network; and iii) using quantized phase shifts [11]. Many authors have addressed these issues using a variety of analytical [12]–[15] and numerical tools [10], [14]–[19]. Most analytical methods make use of the fact that any digital beamforming vector may be implemented by a fully connected hybrid beamformer using continuous phase shifters and two front ends [12]. Actually, only a single front end per data stream is sufficient, if the number of phase shifters per front end is doubled [13]–[15]. However, these results are not applicable if the number of streams is greater than the number of front ends, or if the phase shifters are quantized. Consequently, several numerical approaches to solve the hybrid beamforming problem have been proposed, including alternating minimization [10], [16], majorization-minimization [19], quasi-Newton methods [18], Wirtinger calculus [20], coordinate descent [17], and various heuristics [14], [15].

A. Contributions and organization of paper

The aforementioned works mainly consider hybrid beamforming in a mmWave MIMO communications context. In contrast, this paper proposes a hybrid beamforming phased array architecture for active sensing applications. The co-located transmitting and receiving arrays have a fully connected hybrid architecture and may be sparse. Furthermore, we utilize image addition to synthesize PSFs that are usually only achieved by uniform arrays employing fully digital beamforming. To the best of our knowledge, the resulting multi-image joint transmit-receive beampattern matching problem has not been studied before. In particular, it essentially differs from the typical hybrid beamformer design problem, where the optimization of the transmitter and receiver is decoupled, and spectral efficiency is used as the objective function [21].

The main contributions of the paper are threefold:

- 1) We formulate an optimization problem to jointly find the hybrid transmit and receive beamformers achieving a desired PSF using as few component images as possible.
- 2) We develop a greedy algorithm for approximately solving this non-convex hybrid beamformer design problem. In the special case of the fully digital beamformer, we propose using an alternating minimization algorithm, which is also partly utilized in the hybrid case.
- 3) We derive closed-form beamforming weights yielding upper bounds on the number of component images required by the hybrid and fully analog beamformers to match the beampattern of the fully digital beamformer.

We address the general case when the analog beamforming network consists of phase shifters with quantized phases. In a related work, we study the special case of a single front end connected to phase shifters with continuous phases [22].

The paper is organized as follows. Section II introduces the signal model and defines key concepts, such as the point spread function and the image addition method. Section III formulates the hybrid beamformer weight optimization problem. Section IV reviews key prior work that will be utilized in Section V, where we propose algorithms for approximately solving the hybrid beamforming problem in both the fully digital and hybrid cases. Section VI develops closed-form expressions for the hybrid beamforming weights, which provide upper bounds on the number of component images in the case of continuous and discrete phase shifts. Finally, Section VII demonstrates the performance of the proposed solutions via simulations using both linear and planar arrays. In particular, we show that sparse hybrid beamformers with quantized phase shifters can achieve image quality comparable to uniform fully digital beamformers, at the expense of an increase in the number of transmissions and a reduction in array gain.

B. Notation

Matrices are denoted using bold uppercase, vectors using bold lowercase, and scalars using unbolded letters. The (n, m) th element of matrix \mathbf{A} is denoted as A_{nm} . If the matrix is indexed by a subscript, say as \mathbf{A}_i , the (n, m) th element is denoted as $[\mathbf{A}_i]_{nm}$. Furthermore, the n th row and m th column of matrix \mathbf{A} are denoted as $\mathbf{A}_{n,:}$ and $\mathbf{A}_{:,m}$. Subscripts “t” and “r” denote transmitter and receiver, respectively. We omit these subscripts, or use “x” to indicate either of them to avoid unnecessary repetition whenever possible. The N -dimensional vector of ones is denoted by $\mathbf{1}_N$, and the $N \times N$ identity matrix by \mathbf{I}_N (subscripts are omitted when the dimensions are clear from the context). The standard unit vector, consisting of zeros except for the i th entry, which is unity, is denoted by \mathbf{e}_i (dimension specified separately). The indicator function is denoted by $\mathbb{1}(\cdot)$. The ℓ_p and Frobenius norms are, respectively, denoted as $\|\cdot\|_p$ and $\|\cdot\|_F$, where $p \geq 1$. Operators $(\cdot)^T$, $(\cdot)^H$, $(\cdot)^*$, and $(\cdot)^\dagger$, respectively, denote the matrix transpose, complex conjugate transpose, complex conjugate, and pseudo-inverse. The Kronecker and Khatri-Rao products are denoted by \otimes and \odot . The $\text{vec}(\cdot)$ operator stacks the columns of its matrix argument into a column vector, whereas, $\text{mat}_{N \times M}(\cdot)$ reshapes an NM dimensional vector into a $N \times M$ matrix. The $\text{diag}(\cdot)$ operator constructs a diagonal matrix of its vector argument. Basic operations, such as rounding to the nearest integer $\lceil \cdot \rceil$ or the angle of a complex-valued number $\angle \cdot$, are applied

TABLE I: Frequently used symbols. Subscript “x” denotes either the receiver (“r”) or transmitter (“t”).

Symbol	Description
N_x	No. of array elements
M_x	No. of front ends
B	No. of bits (per phase shifter)
Q	No. of component images
V	No. of spatial sampling directions (angles)
N_Σ	No. of sum co-array elements

elementwise to matrix arguments. Table I lists the symbols that are referred most frequently in the text.

II. SIGNAL MODEL AND DEFINITIONS

In this section, we introduce the signal model and key definitions. In particular, we consider active narrowband sensing of coherent far-field point scatterers using linear processing at both the transmitter and receiver. We first define matrix \mathbf{F}_x , which models the analog beamforming network consisting of phase shifters. We then briefly recall the key concept of the point spread function, which characterizes the performance of a linear imaging system. We also review the image addition method that extends the set of point spread functions that are achievable by hybrid or sparse arrays. Finally, we introduce the sum co-array, which is fundamental in determining the set of achievable point spread functions.

A. Signal model

Consider a phased planar array imaging system that sequentially scans a scattering scene by transmitting and receiving focused beams of narrowband signals. Such systems are typically used in, e.g., medical ultrasound imaging or radar. Let N_t denote the number of transmitting (Tx) and N_r the number of receiving (Rx) array elements. The number of Tx and Rx front ends are reduced using analog preprocessing networks comprising of phase shifters, as shown in Fig. 1. Specifically, we use a bank of $M_t \leq N_t$ Tx front ends and $M_r \leq N_r$ Rx front ends. We refer to the beamforming architecture as

- *fully digital*, when $M_x = N_x$

- *hybrid*, when $2 \leq M_x < N_x$
- *fully analog*, when $M_x = 1$.

Both the hybrid and analog architectures are assumed to be fully connected, whereas the digital architecture is partially connected, since each sensor has a dedicated front end.

We transmit a modulated narrowband pulse using the transmit beamforming weights $\mathbf{w}_t = \mathbf{F}_t \mathbf{c}_t \in \mathbb{C}^{N_t}$, where $\mathbf{c}_t \in \mathbb{C}^{M_t}$ denotes the digital weight vector, and $\mathbf{F}_t \in \mathbb{C}^{N_t \times M_t}$ the analog phase shift matrix (see section II-B for details). The transmitted radiation is reflected off scatterers in the field-of-view of the transmit array and observed by the receiver, where it is processed by a hybrid beamforming network with the beamforming weights $\mathbf{w}_r = \mathbf{F}_r \mathbf{c}_r \in \mathbb{C}^{N_r}$. Here $\mathbf{c}_r \in \mathbb{C}^{M_r}$ denotes the digital, and $\mathbf{F}_r \in \mathbb{C}^{N_r \times M_r}$ the analog beamforming weights of the receiver. The beamformed signal is then processed using a digital matched filter yielding

$$y(\mathbf{u}) = \mathbf{w}_r^T(\mathbf{u}) \mathbf{A}_r \mathbf{\Gamma} \mathbf{A}_t^T \mathbf{w}_t(\mathbf{u}) + \mathbf{w}_r^T(\mathbf{u}) \mathbf{n}, \quad (1)$$

where $\mathbf{u} \in \mathbb{R}^3$ is the scan direction taking the form $\mathbf{u} = [\sin \varphi \sin \theta, \cos \varphi \sin \theta, \cos \theta]^T$, when the array is focused in the far-field. Here $\varphi \in [-\pi/2, \pi/2]$ and $\theta \in [0, \pi]$ are the azimuth and elevation angles of the scan direction, respectively. Matrix $\mathbf{\Gamma} = \text{diag}(\boldsymbol{\gamma}) \in \mathbb{C}^{K \times K}$ is a diagonal matrix, with $\boldsymbol{\gamma} = [\gamma_1, \dots, \gamma_K]^T \in \mathbb{C}^K$ containing the scattering coefficients of the K reflectors, and $\mathbf{n} \in \mathbb{C}^{N_r}$ is a vector of spatio-temporally white complex circular Gaussian noise with zero mean and covariance matrix $\sigma^2 \mathbf{I}$. Furthermore, the $N_x \times K$ steering matrix of the Tx or Rx array is

$$\mathbf{A}_x = [\mathbf{a}_x(\mathbf{v}_1), \dots, \mathbf{a}_x(\mathbf{v}_K)], \quad (2)$$

where the steering vector $\mathbf{a}_x(\mathbf{v}_k) \in \mathbb{C}^{N_x}$ is evaluated in scatterer direction $\{\mathbf{v}_k \in \mathbb{R}^3\}_{k=1}^K$. When the scatterers are located in the far-field of both the transmitting and receiving array, we have $\mathbf{v}_k = [\sin \varphi_k \sin \theta_k, \cos \varphi_k \sin \theta_k, \cos \theta_k]^T$, where $\varphi_k \in [-\pi/2, \pi/2]$ and $\theta_k \in [0, \pi]$ denote the azimuth and elevation angles of the k th scatterer. Eq. (1), or its magnitude $|y(\mathbf{u})|$, may be interpreted as an image of the scattering scene. Typically, this image is evaluated for a discrete set of steering directions, i.e., pixels.

B. Analog phase shift matrix \mathbf{F}_x

The entries of the analog phase shift matrix $\mathbf{F}_x \in \mathcal{F}_x(B)$ are complex exponentials with discrete phases. Specifically, let

$$\mathcal{F}_x(B) = \{\mathbf{F} = \exp(j\Phi) \mid \Phi \in \mathbb{R}^{N_x \times M_x}, \Phi_{nm} \in \Phi(B)\}, \quad (3)$$

$$\Phi(B) = \{0, 2\pi/2^B, \dots, (2^B - 1)2\pi/2^B\}, \quad (4)$$

where the exponential function in (3) is applied elementwise, and B denotes the number of bits used to uniformly quantize the phase of each entry of \mathbf{F} over the interval $[0, 2\pi)$. Note that (4) ensures that $\Phi(B+1) \supset \Phi(B)$, and thereby $\mathcal{F}_x(B+1) \supset \mathcal{F}_x(B)$. It also follows from (4) that the phase quantization operator $\mathcal{P}_B(\Psi)$, i.e., the projection of the elements of some matrix $\Psi \in [0, 2\pi)^{N \times M}$ to set $\Phi(B)$, can be expressed as

$$\mathcal{P}_B(\Psi) = \frac{\pi}{2^{B-1}} \left\lceil \frac{2^{B-1}}{\pi} \Psi \right\rceil \bmod 2\pi. \quad (5)$$

Letting the number of bits go to infinity yields the special case of continuous phase shifters: $\mathcal{F}_x(\infty) = \lim_{B \rightarrow \infty} \mathcal{F}_x(B)$; $\Phi(\infty) = \lim_{B \rightarrow \infty} \Phi(B) = [0, 2\pi)$; and $\mathcal{P}_\infty(\Psi) = \Psi$.

C. Point spread function

The *point spread function* (PSF) fully defines the spatial impulse response of a linear imaging system, and is key in characterizing the achievable resolution and interference suppression capability. The effective PSF of an active array is the product of the Tx and Rx PSFs, as illustrated in Fig. 2. Specifically, for the array focused in the direction $\mathbf{u} \in \mathbb{R}^3$, and a unit reflectivity point-scatterer in the direction $\mathbf{v} \in \mathbb{R}^3$, the PSF is defined as

$$\psi(\mathbf{u}, \mathbf{v}) = (\mathbf{a}_t(\mathbf{v}) \otimes \mathbf{a}_r(\mathbf{v}))^T \text{vec}(\mathbf{W}(\mathbf{u})),$$

where $\mathbf{W}(\mathbf{u}) = \mathbf{w}_r(\mathbf{u})\mathbf{w}_t^T(\mathbf{u}) \in \mathbb{C}^{N_r \times N_t}$ is a rank-1 matrix. For a fixed \mathbf{u} and a discrete set of V scatterer directions $\{\mathbf{v}_i\}_{i=1}^V$ determined by the desired imaging region and resolution, the PSF may be expressed as a vector $\psi \in \mathbb{C}^V$ satisfying

$$\psi = \mathbf{A}^T \text{vec}(\mathbf{W}). \quad (6)$$

Here the i th column of the *effective steering matrix* $\mathbf{A} \in \mathbb{C}^{N_r N_t \times V}$ is given by the Kronecker product of the Tx and Rx steering vectors evaluated in direction \mathbf{v}_i , i.e., $\mathbf{a}_t(\mathbf{v}_i) \otimes \mathbf{a}_r(\mathbf{v}_i)$.

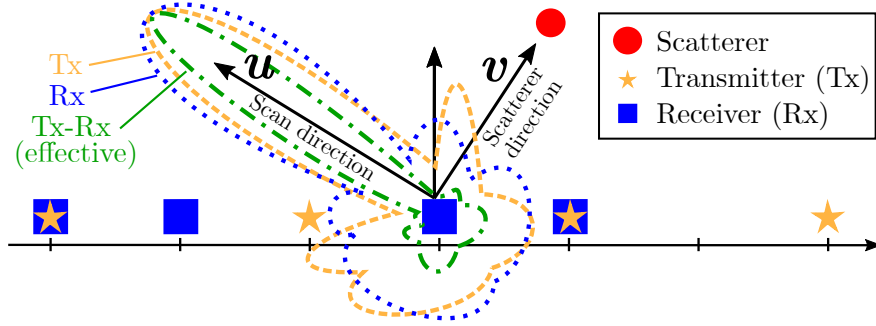


Fig. 2: The PSF is the spatial response of the array to a point scatterer in direction \mathbf{v} , with the array steered in direction \mathbf{u} . The effective PSF is the product of the Tx and Rx array PSFs.

Consequently, \mathbf{A} can be expressed as the Khatri-Rao product of the Tx and Rx steering matrices $\mathbf{A}_x \in \mathbb{C}^{N_x \times V}$ in (2):

$$\mathbf{A} = \mathbf{A}_t \odot \mathbf{A}_r. \quad (7)$$

Any feasible PSF ψ thus lies in the row space of \mathbf{A} . For examples of typical PSFs, see Section VII-A4.

D. Image addition

A single Tx-Rx weight pair $\{\mathbf{w}_t, \mathbf{w}_r\}$ may not always suffice to achieve a desired PSF. In this case, the range of feasible PSFs may be extended by *image addition* [2]. Image addition synthesizes a composite image with improved resolution and lower side lobe levels, by summing together several *component images* that are formed using different Tx-Rx weight pairs. This corresponds to using a rank- Q *co-array weight matrix* $\mathbf{W} \in \mathbb{C}^{N_r \times N_t}$ in (6), defined as [23]:

$$\mathbf{W} = \sum_{q=1}^Q \mathbf{w}_{r,q} \mathbf{w}_{t,q}^T = \mathbf{W}_r \mathbf{W}_t^T, \quad (8)$$

where $\mathbf{W}_x = [\mathbf{w}_{x,1}, \dots, \mathbf{w}_{x,Q}] \in \mathbb{C}^{N_x \times Q}$. Each rank-1 matrix $\mathbf{w}_{r,q} \mathbf{w}_{t,q}^T$ in (8) corresponds to a transmission and reception with a different pair of Tx and Rx weight vectors $\mathbf{w}_{t,q}$ and $\mathbf{w}_{r,q}$. These vectors may be found from the *singular value decomposition* (SVD) of matrix \mathbf{W} in the case of a fully digital beamformer [23]. The smaller the *number of component images* Q is, the

shorter the image acquisition time, since fewer transmissions are required in forming an image. In the case of hybrid beamforming, (8) becomes

$$\mathbf{W} = \sum_{q=1}^Q \mathbf{F}_{r,q} \mathbf{c}_{r,q} \mathbf{c}_{t,q}^T \mathbf{F}_{t,q}^T = \mathbf{F}_r (\mathbf{I} \odot \mathbf{C}_r) (\mathbf{I} \odot \mathbf{C}_t)^T \mathbf{F}_t^T, \quad (9)$$

where matrices $\mathbf{F}_x = [\mathbf{F}_{x,1}, \dots, \mathbf{F}_{x,Q}] \in \mathcal{F}_x(B) \subset \mathbb{C}^{N_x \times M_x Q}$ and $\mathbf{C}_x = [\mathbf{c}_{x,1}, \dots, \mathbf{c}_{x,Q}] \in \mathbb{C}^{M_x \times Q}$, respectively, contain the analog and digital beamforming weights of all the Q component images. Note that (9) is not necessarily unique, as is shown in Section VI-B1. Furthermore, although $\mathbf{c}_{x,q}$ could also be defined as a real-valued vector, allowing for complex-valued entries is more convenient for our purposes.

E. Sum co-array

The sum co-array, \mathcal{D}_Σ , is a virtual array structure defined as the set of pairwise sums of the transmit and receive element positions $\mathcal{D}_x = \{\mathbf{d}_{x,1}, \dots, \mathbf{d}_{x,N_x}\} \subset \mathbb{R}^3$:

$$\mathcal{D}_\Sigma = \{\mathbf{d}_t + \mathbf{d}_r \mid \mathbf{d}_x \in \mathcal{D}_x\}. \quad (10)$$

The sum co-array ultimately determines the set of PSFs that the array can achieve [2]. The utility of the sum co-array stems from the fact that it has at least as many virtual elements $N_\Sigma = |\mathcal{D}_\Sigma|$ as either of the physical arrays, since $N_\Sigma \geq N_t + N_r - 1$. If the transceivers are co-located, that is, $\mathcal{D}_t = \mathcal{D}_r$ and $N_x = N$, a simple counting argument shows that $N_\Sigma \leq N(N+1)/2$. The array is redundant if $N_\Sigma < N(N+1)/2$. If the transmitting and receiving elements can be placed independently of each other, the redundancy condition is $N_\Sigma < N_t N_r$.

Steering matrix \mathbf{A} in (7) may have fewer than $N_t N_r$ unique rows when the array configuration is redundant. In particular, the number of unique rows equals the number of sum co-array elements N_Σ , for example, when the array elements are identical and mutual coupling is negligible. The unique rows of \mathbf{A} are therefore contained in the *sum co-array steering matrix* $\mathbf{A}_\Sigma \in \mathbb{C}^{N_\Sigma \times V}$ satisfying

$$\mathbf{A} = \mathbf{\Upsilon}^T \mathbf{A}_\Sigma. \quad (11)$$

Here $\mathbf{\Upsilon}$ is an $N_\Sigma \times N_t N_r$ binary matrix mapping the set of virtual elements arising from the Kronecker structure in (7) to the set of sum co-array elements in (10). The sum co-array and the multiplicities of its element uniquely determine $\mathbf{\Upsilon}$.

Definition 1 (Sum co-array selection matrix). Map $\Upsilon : \mathbb{C}^{N_t N_r} \mapsto \mathbb{C}^{N_\Sigma}$ is a binary matrix $\Upsilon \in \{0, 1\}^{N_\Sigma \times N_t N_r}$, where

$$\Upsilon_{n,m} = \begin{cases} 1, & \text{if } \mathbf{d}_{\Sigma,n} = \mathbf{d}_{t,\lceil m/N_r \rceil} + \mathbf{d}_{r,1+(m-1) \bmod N_r} \\ 0, & \text{otherwise.} \end{cases}$$

Here $\mathbf{d}_{x,i} \in \mathcal{D}_x$ denote the elements of the physical array and $\mathbf{d}_{\Sigma,n} \in \mathcal{D}_\Sigma$ the elements of the sum co-array.

Any feasible PSF may be expressed as $\boldsymbol{\psi} = \mathbf{A}_\Sigma^T \mathbf{w}_\Sigma$, where

$$\mathbf{w}_\Sigma = \Upsilon \text{vec}(\mathbf{W}) \quad (12)$$

is the N_Σ -dimensional *sum co-array beamforming weight vector*. Note that if $V < N_\Sigma$, then (12) is only sufficient for satisfying (6). If $\text{rank}(\mathbf{A}_\Sigma) = N_\Sigma$, which holds only if $V \geq N_\Sigma$, then (12) is also necessary. When the physical array is a uniform array with N co-located transceivers, then $N_\Sigma \propto N$. Conversely, a sparse array may have $N_\Sigma \propto N^2$. Consequently, these arrays would typically require (at least) $V \propto N$, respectively, $V \propto N^2$ angular samples.

III. PROBLEM FORMULATION

In this section, we formulate the hybrid beamformer weight optimization problem as a spatial filter design problem. Our fidelity measure of choice is the ℓ_2 approximation error

$$\varepsilon = \|\boldsymbol{\psi} - \mathbf{A}^T \text{vec}(\mathbf{W})\|_2^2.$$

Here $\boldsymbol{\psi} \in \mathbb{C}^V$ is the desired PSF (sampled in V directions), which is also assumed to be feasible (in the row space of \mathbf{A}). The realized PSF $\mathbf{A}^T \text{vec}(\mathbf{W})$ is determined by the measurement (or steering) matrix \mathbf{A} given by (7), and the co-array weight matrix $\mathbf{W} \in \mathbb{C}^{N_r \times N_t}$, which factorizes as (9).

The objective is to minimize the number of component images Q , while achieving a desired PSF. This leads to the following non-convex optimization problem¹:

$$\begin{aligned} & \text{minimize} && Q \\ & \{\mathbf{F}_{x,q} \in \mathcal{F}_x(B), \mathbf{c}_{x,q} \in \mathbb{C}^{M_x}\}_{q=1}^{Q \in \mathbb{N}_+} \\ & \text{subject to} && \left\| \boldsymbol{\psi} - \mathbf{A}^T \text{vec} \left(\sum_{q=1}^Q \mathbf{F}_{r,q} \mathbf{c}_{r,q} \mathbf{c}_{t,q}^T \mathbf{F}_{t,q}^T \right) \right\|_2^2 \leq \varepsilon_{\max}. \end{aligned} \quad (\text{P1})$$

In (P1), $\varepsilon_{\max} \geq 0$ is an approximation error tolerance parameter, and \mathcal{F}_x denotes the analog weight matrix constraint set in (3). The fact that Q is unknown further complicates problem (P1). If we instead fix Q , we obtain the following slightly simpler optimization problem:

$$\begin{aligned} & \text{minimize} && \left\| \boldsymbol{\psi} - \mathbf{A}^T \text{vec} \left(\sum_{q=1}^Q \mathbf{F}_{r,q} \mathbf{c}_{r,q} \mathbf{c}_{t,q}^T \mathbf{F}_{t,q}^T \right) \right\|_2^2 \\ & \{\mathbf{F}_{x,q} \in \mathcal{F}_x(B), \\ & \mathbf{c}_{x,q} \in \mathbb{C}^{M_x}\}_{q=1}^Q \end{aligned} \quad (\text{P2})$$

Note that Q determines the number of optimization variables in both optimization problems, which implies that the optimal value of the objective function of (P2) is non-increasing in Q . We may therefore recover the solution to (P1) from (P2) by finding the smallest Q for which the objective function of (P2) does not exceed the approximation error tolerance ε_{\max} . This can easily be accomplished using binary search (bisection) at a small additional cost, given a search interval of feasible values of Q . Consequently, we will henceforth focus on (P2) instead of (P1). If we know the weight vectors $\mathbf{w}_{x,q} \in \mathbb{C}^N$, which may be the case when a fully digital solution is available, we may solve the even simpler optimization problem

$$\begin{aligned} & \text{minimize} && \|\mathbf{w} - \mathbf{F}\mathbf{c}\|_2^2 \\ & \mathbf{F} \in \mathcal{F}(B), \mathbf{c} \in \mathbb{C}^M \end{aligned} \quad (\text{P3})$$

independently for the transmitter, receiver, and each component image (we omit the subscripts in (P3) for simplicity). Problem (P3) recovers a hybrid solution to (P1), if a fully digital solution to (P1) is available, and if this solution can be factorized as in (9) for the same number of component images as in the fully digital case. However, since this is generally not the case, (P2) needs to be solved instead.

¹We do not constrain the transmit power for simplicity. However, the Rx and Tx weight vectors are normalized post optimization as $\mathbf{w}_{r,q} \leftarrow \mathbf{w}_{r,q} / \|\mathbf{w}_{r,q}\|_\infty$ and $\mathbf{w}_{t,q} \leftarrow \mathbf{w}_{t,q} / \|\mathbf{w}_{t,q}\|_\infty^{-1}$ to ensure that the transmitters are operated at saturation and SNR is maximized for each of the Q component images.

IV. KEY RESULTS IN PRIOR WORK

In this section, we review two key results (used in Sections V and VI) related to solving optimization problem (P3) using hybrid and analog beamformers with continuous phase shifters. We again omit subscripts x and q for simplicity, since the results are independently applicable to both the transmitter and receiver, as well as any component image.

Zhang et al. [12] showed that two front ends with continuous phase shifts are sufficient for factorizing any $\mathbf{w} \in \mathbb{C}^N$ as $\mathbf{w} = \mathbf{F}\mathbf{c}$, thus optimally solving (P3) when $M \geq 2$. The hybrid beamforming weights can also be expressed in closed form, as shown by the following lemma adapted² from [12].

Lemma 1 (Solution to (P3) using two front ends and continuous phase shifters [12]). *Let $M=2$ and $B \rightarrow \infty$. Given any $\mathbf{w} \in \mathbb{C}^N$, an optimal solution to (P3) achieving $\mathbf{w} = \mathbf{F}\mathbf{c}$, where $\mathbf{c} \in \mathbb{C}^2$ and $\mathbf{F} \in \mathcal{F}(\infty)$ following (3), is given by*

$$\mathbf{F} = \exp \left(j \left(\angle \mathbf{w} \mathbf{1}_2^T + \cos^{-1} \left(\frac{|\mathbf{w}|}{\|\mathbf{w}\|_\infty} \right) (\mathbf{1}_2 - 2\mathbf{e}_2)^T \right) \right) \quad (13)$$

$$\mathbf{c} = \frac{\|\mathbf{w}\|_\infty}{2} \mathbf{1}_2. \quad (14)$$

Here $\mathbf{1}_2$ is a vector of ones, \mathbf{e}_2 is the standard unit vector, and \cos^{-1} , $|\cdot|$, and the angle operator \angle are applied elementwise.

Proof. See Appendix A.

Fig. 3 illustrates Lemma 1, showing how each entry $w_n \in \mathbb{C}$ of vector $\mathbf{w} \in \mathbb{C}^N$ can be expressed as the sum of two phasors with magnitude $\|\mathbf{w}\|_\infty/2$ and phases depending on w_n and $\|\mathbf{w}\|_\infty$. Note that (13) and (14) are not unique, since any $c_1 = c_2 \geq \|\mathbf{w}\|_\infty/2$ yields a feasible factorization $\mathbf{w} = \mathbf{F}\mathbf{c}$. In general, unequal magnitudes $|c_1| \neq |c_2|$ are also possible if $\min_n |w_n| > 0$ holds (see Appendix A). We may also easily extend Lemma 1 to the case $M > 2$ by appending zeros to \mathbf{c} and columns with arbitrary phases to \mathbf{F} [12].

Lemma 1 implies that the number of front ends M required to implement any fully digital weight vector $\mathbf{w} \in \mathbb{C}^N$ is independent of the number of array elements N , provided continuous phase shifts are used. The number of front ends may actually be reduced to just one, if the

²This is a reformulation of [12, Theorem 1 and Appendix A], where we give a slightly more general expression for the phase of \mathbf{F} in Appendix A.

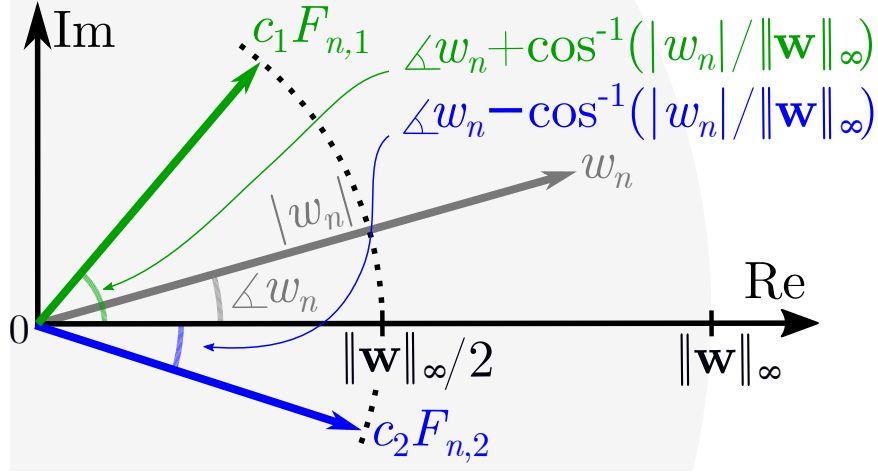


Fig. 3: Illustration of Lemma 1. Any point within the shaded disk can be expressed as the sum of two phasors with fixed equal magnitudes and appropriately chosen phases.

digital weight vector $\mathbf{c} \in \mathbb{C}^M$ can be selected as the scaled unit vector $\mathbf{c} = c\mathbf{1}_M$, where $c \in \mathbb{C}$ [13]–[15], as in (14). However, a modification to the canonical fully-connected architecture is required. Namely, all MN phase shifters need to be connected to a single front end, as explained in the following remark.

Remark 1 (Analog beamformer with modified architecture [13]–[15]). *Consider a fully connected hybrid beamformer with M front ends connected to N phase shifters each. If $\mathbf{c} = c\mathbf{1}_M, c \in \mathbb{C}$, we may form an equivalent analog beamformer with a single front end connected to all NM phase shifters.*

Perfect factorization of \mathbf{w} is not generally possible, if $M = 1$ and the number of phase shifters equals the number of array elements N . Nevertheless, (P3) actually admits a closed-form solution when $B \rightarrow \infty$, as shown by the following lemma.

Lemma 2 (Solution to (P3) using single front end and continuous phase shifters). *Let $M = 1$ and $B \rightarrow \infty$. Given any $\mathbf{w} \in \mathbb{C}^N$, an optimal solution to (P3) that minimizes $\|\mathbf{w} - \mathbf{c}\mathbf{f}\|_2^2$, where $c \in \mathbb{C}$ and $\mathbf{f} \in \mathcal{F}(\infty)$ following (3), is given by*

$$\mathbf{f} = \exp(j\angle \mathbf{w}) \quad (15)$$

$$c = \|\mathbf{w}\|_1 / N. \quad (16)$$

Furthermore, the optimal value of (P3) is $\|\mathbf{w}\|_2^2 - \|\mathbf{w}\|_1^2 / N$.

Proof. See Appendix B.

In general, Lemma 2 only yields an approximate factorization $\mathbf{w} \approx c\mathbf{f}$. Equality $\mathbf{w} = c\mathbf{f}$ holds if and only if the entries of \mathbf{w} have equal magnitude, i.e., $|w_1| = |w_2| = \dots = |w_N|$.

V. ALGORITHMS FOR FINDING BEAMFORMER WEIGHTS

In this section, we develop three algorithms for approximately solving optimization problems (P2) and (P3). In the fully digital beamforming case, we address (P2) using alternating minimization (Algorithm 1). In the hybrid and analog beamforming cases, we use a greedy approach to approximately solve both (P3) (Algorithm 2) and (P2) (Algorithm 3). Table II summarizes the proposed algorithms.

TABLE II: Summary of beamformer weight optimization algorithms proposed in Section V.

Algorithm	Beamforming architecture	Problem	Worst case complexity ^a $\mathcal{O}(\cdot)$	Explanation
1	Digital	(P4)	$k_{\max} V Q N \max(V, Q N)$	Alternating minimization
2	Hybrid or Analog	(P3)	$M^2 N^2$	Greedy + Lemma 1 and 2
3	Hybrid or Analog	(P2)	$k_{\max} V Q \max(NV, MQV, M^2 Q^2) + Q N^2 M^2$	Greedy + Algorithm 1 and 2 + Alt. min.

^a Assuming $N_x \propto N$; $M_x \propto M$; and $V \geq N$.

A. Fully digital beamformer

The fully digital beamformer serves as a natural baseline for the hybrid beamformer. This is because the digital beamformer imposes the fewest constraints on the solutions to the optimization problems in Section III. In the following, we develop an alternating minimization algorithm for solving (P2) in the fully digital case. We will also utilize this algorithm in the hybrid case developed in Section V-B.

1) *Alternating minimization:* Digital beamformer design is substantially simplified by the absence of phase shifters, which reduces (P2) to the following biconvex problem

$$\underset{\mathbf{W}_x \in \mathbb{C}^{N_x \times Q}}{\text{minimize}} \|\boldsymbol{\psi} - \mathbf{A}^T \text{vec}(\mathbf{W}_r \mathbf{W}_t^T)\|_2^2. \quad (\text{P4})$$

Here the columns of $\mathbf{W}_x = [\mathbf{w}_{x,1}, \mathbf{w}_{x,2}, \dots, \mathbf{w}_{x,Q}] \in \mathbb{C}^{N_x \times Q}$ are the unknown weight vectors, each corresponding to a specific component image. Problem (P4) is non-convex due to the product of the unknown matrices \mathbf{W}_r and \mathbf{W}_t . However, we may find a local minimum of (P4) in a straightforward fashion by *alternating minimization*. The *low rank matrix sensing problem* (P4) was actually studied by Jain et. al [24] in a more general (albeit real-valued) setting. Next,

Algorithm 1 Digital beamformer: alternating min. for (P4)

```

1: procedure ALTMIN( $\mathbf{A}, \boldsymbol{\psi}, Q, k_{\max}, \varepsilon_{\max}$ )
2:    $\mathbf{W} \leftarrow \sum_{v=1}^V \psi_v \text{mat}_{N_r \times N_t}(\mathbf{A}_{:,v})$  ▷ initialization [24]
3:    $\{\mathbf{U}, \boldsymbol{\Sigma}, \mathbf{V}\} \leftarrow \text{SVD}(\mathbf{W}, Q)$  ▷  $Q$  princ. components
4:    $\{\mathbf{W}_t, k, \varepsilon\} \leftarrow \{\mathbf{V}^*, 0, \infty\}$ 
5:   while  $k < k_{\max} \wedge \varepsilon > \varepsilon_{\max}$  do
6:     Update  $\mathbf{W}_r$  and  $\mathbf{W}_t$  using (17) and (18)
7:      $\varepsilon \leftarrow \|\boldsymbol{\psi} - \mathbf{A}^T \text{vec}(\mathbf{W}_r \mathbf{W}_t^T)\|_2^2$ 
8:      $k \leftarrow k + 1$ 
9:   return  $\mathbf{W}_r, \mathbf{W}_t$ 

```

we describe in detail a slightly modified version of their ‘‘AltMinSense’’ algorithm, adapted to the beamforming application considered in this paper. The alternating minimization algorithm, summarized in Algorithm 1, starts with an initial guess for \mathbf{W}_t and proceeds by computing the least squares solutions:

$$\mathbf{W}_r = \text{mat}_{N_r \times Q}((\mathbf{A}^T(\mathbf{W}_t \otimes \mathbf{I}_{N_r}))^\dagger \boldsymbol{\psi}) \quad (17)$$

$$\mathbf{W}_t = \text{mat}_{Q \times N_t}^T((\mathbf{A}^T(\mathbf{I}_{N_t} \otimes \mathbf{W}_r))^\dagger \boldsymbol{\psi}). \quad (18)$$

Equations (18) and (17) are iteratively solved until a desired error ε_{\max} or maximum number of iterations k_{\max} is achieved. Although alternating minimization is guaranteed to converge to a local minimum, which local minimum is found depends on the initialization. We choose to use the spectral initialization $\mathbf{W} = \sum_{v=1}^V \psi_v \mathbf{a}_{r,v} \mathbf{a}_{t,v}^T = \sum_{v=1}^V \psi_v \text{mat}_{N_r \times N_t}(\mathbf{A}_{:,v})$ to confine the initialization to the solution subspace [24]. We then initialize \mathbf{W}_t using the right singular vectors corresponding to the Q largest singular values of \mathbf{W} . Alternatively, multiple different initializations of \mathbf{W}_t could be used to increase the chances of finding a good local, or even global, minimum. Note that when $Q = \min(N_r, N_t)$, we may simply obtain \mathbf{W}_t and \mathbf{W}_r from the SVD of the least squares solution $\mathbf{W} = \text{mat}_{N_r \times N_t}((\mathbf{A}^T)^\dagger \boldsymbol{\psi})$.

2) *Worst-case complexity*: The most expensive operation in Algorithm 1 is on line 6, where the worst-case time complexity of computing the pseudo-inverse is proportional to that of the SVD. In general, the SVD of a full m by n matrix has complexity $\mathcal{O}(m^2n)$, where $m \geq n$ [25, p. 493]. The worst-case complexity of Algorithm 1 is therefore $\mathcal{O}(k_{\max} m^2n)$, where $m =$

$\max(V, QN_{\max})$, $n = \min(V, QN_{\max})$, and $N_{\max} = \max(N_r, N_t)$. Assuming that $N_x \propto N$, the complexity of Algorithm 1 simplifies to

$$\mathcal{O}(k_{\max} V Q N \max(V, QN)).$$

As indicated in Section II-E, typically $V \propto N$ for a uniform array, and $V \propto N^2$ for a sparse array. This simplifies the complexity of Algorithm 1 to $\mathcal{O}(k_{\max} Q^2 N^3)$, or $\mathcal{O}(k_{\max} Q N^5)$, respectively. In either case, the complexity is at most on the order of N^5 or N^6 , since $Q \leq N$. This may become prohibitively large for an array with hundreds of elements. Note that the number of iterations $k \leq k_{\max}$ required by Algorithm 1 also depends on the properties of matrix \mathbf{A} and the desired error tolerance ε_{\max} [24]. A more detailed complexity analysis is however out of the scope of this paper.

B. Hybrid beamformer

We will show in Section VI that it is possible to construct a hybrid beamformer that solves (P1) using continuous phase shifts and exactly two front ends, if a fully digital solution to (P1) is given. In case of discrete phase shifts, it may be sufficient to quantize this hybrid solution, provided that the number of phase shift bits is sufficiently large. However, poor results may follow if too few bits are used [14]. Furthermore, this approach does not benefit from increasing $M_x > 2$.

1) *Greedy subroutine:* As a first step towards addressing the issues outlined above, we consider problem (P3), and adopt a greedy method in Algorithm 2 to approximately solve it. Starting with a fully digital solution \mathbf{w} , we initialize the residual as $\mathbf{w}' = \mathbf{w}$, and apply Lemma 1 to find $\mathbf{F} \in \mathcal{F}(\infty) \subset \mathbb{C}^{N \times 2}$ satisfying $\mathbf{w}' = \mathbf{F} \mathbf{1}_2 \|\mathbf{w}'\|_{\infty} / 2$. Using (5), we quantize the phase of \mathbf{F} , yielding $\mathbf{F} = \exp(j\mathcal{P}_B(\angle \mathbf{F})) \in \mathcal{F}(B) \subset \mathbb{C}^{N \times 2}$. We then compute the least squares solution of the digital weights \mathbf{c} before updating the residual on line 7. The process is repeated a total of $\lfloor M/2 \rfloor$ times. In case M is odd, we quantize the analog least squares solution given by Lemma 2 in the final iteration. The solution found by Algorithm 2 becomes exact, i.e., $\mathbf{w}' \rightarrow 0$, when either (i) $B \geq 1, M \rightarrow \infty$, or (ii) $B \rightarrow \infty, M \geq 2$. We note that Algorithm 2 is similar to [20, Algorithm 1], although we consider a different problem with quantized phase shifts, as well as utilize Lemma 1. Other algorithms addressing (P3), or modifications thereof, also exist [17]. However, solving (P3) alone is insufficient for solving the problem of interest (P2), as we will show next. A detailed comparison of alternatives to Algorithm 2 is therefore beyond the scope of this paper and left for future work.

Algorithm 2 Hybrid beamformer: greedy method for (P3)

```

1: procedure GREEDYSUB( $\mathbf{w}$ ,  $M$ ,  $B$ )
2:    $\mathbf{w}' \leftarrow \mathbf{w}$ 
3:   for  $m \in \{1, 2, \dots, \lfloor M/2 \rfloor\}$  do ▷ Lemma 1
4:      $\Phi \leftarrow \angle \mathbf{w}' \mathbf{1}_2^T + \cos^{-1}(\|\mathbf{w}'\|/\|\mathbf{w}'\|_\infty)(\mathbf{1}_2 - 2\mathbf{e}_2)^T$ 
5:      $\mathbf{F}_{:, (2m-1):2m} \leftarrow \exp(j\mathcal{P}_B(\Phi))$  ▷ quantization
6:      $\mathbf{c}_{1:2m} \leftarrow \mathbf{F}_{:, 1:2m}^\dagger \mathbf{w}$  ▷ LS solution
7:      $\mathbf{w}' \leftarrow \mathbf{w} - \mathbf{F}_{:, 1:2m} \mathbf{c}_{1:2m}$  ▷ update residual
8:   if  $M \bmod 2 = 1$  then ▷ Lemma 2
9:      $\mathbf{F}_{:, M} \leftarrow \exp(j\mathcal{P}_B(\angle \mathbf{w}'))$ 
10:     $\mathbf{c} \leftarrow \mathbf{F}^\dagger \mathbf{w}$ 
11:  return  $\mathbf{F}$ ,  $\mathbf{c}$ 

```

2) *Greedy main routine:* If the number of component images of the hybrid beamformer is $Q \leq \text{rank}(\mathbf{W})$, we can directly apply Algorithm 2 to each fully digital weight vector $\{\mathbf{w}_{x,q}\}_{q=1}^{\text{rank}(\mathbf{W})}$ and find an approximate solution to (P2). However, this solution does not improve if Q is increased beyond $\text{rank}(\mathbf{W})$. Consequently, we propose Algorithm 3, which uses Algorithm 1 and 2 to iteratively compute and quantize the rank-1 matrix \mathbf{W} that minimizes the ℓ_2 -norm of the residual PSF vector $\psi' \in \mathbb{C}^V$. The residual is initialized as the desired PSF $\psi' = \psi$, and updated at the end of each iteration by subtracting the q -component realized PSF from ψ . The hybrid weights of the q th iteration $\mathbf{F}_{x,q} \in \mathbb{C}^{N_x \times M_x}$ and $\mathbf{c}_{x,q} \in \mathbb{C}^{M_x}$ are found by applying Algorithm 2 to the fully digital single component solution obtained by calling Algorithm 1 with $Q = 1$. Finally, the digital weights $\{c_{x,l}\}_{l=1}^q$ are recomputed by solving (P2) with \mathbf{F}_x fixed, i.e., the following problem:

$$\underset{\mathbf{C}_x \in \mathbb{C}^{M_x \times q}}{\text{minimize}} \|\psi - \mathbf{A}^T \text{vec}(\mathbf{F}_r(\mathbf{I} \odot \mathbf{C}_r)(\mathbf{I} \odot \mathbf{C}_t)^T \mathbf{F}_t^T)\|_2^2. \quad (\text{P5})$$

Problem (P5) is biconvex, since $\text{vec}(\mathbf{W})$ can be rewritten as

$$\begin{aligned} \text{vec}(\mathbf{W}) &= ((\mathbf{F}_t(\mathbf{I} \odot \mathbf{C}_t) \otimes \mathbf{1}_{M_r}^T) \odot \mathbf{F}_r) \text{vec}(\mathbf{C}_r) \\ &= (\mathbf{F}_t \odot (\mathbf{F}_r(\mathbf{I} \odot \mathbf{C}_r) \otimes \mathbf{1}_{M_r}^T)) \text{vec}(\mathbf{C}_t). \end{aligned}$$

This follows from (9) and the easily verifiable identities (i) $\text{vec}(\mathbf{X}\mathbf{x}\mathbf{y}^T\mathbf{Y}^T) = (\mathbf{Y}\mathbf{y}\mathbf{1}^T \odot \mathbf{X})\mathbf{x} = (\mathbf{Y} \odot \mathbf{X}\mathbf{x}\mathbf{1}^T)\mathbf{y}$, and (ii) $\sum_{l=1}^q \mathbf{Z}_l \mathbf{z}_l = [\mathbf{Z}_1, \dots, \mathbf{Z}_q][\mathbf{z}_1^T, \dots, \mathbf{z}_q^T]^T$ after simplifications. A local minimum of

Algorithm 3 Hybrid beamformer: greedy method for (P2)

```

1: procedure GREEDY( $\mathbf{A}, \boldsymbol{\psi}, M_r, M_t, B, Q, k_{\max}, \varepsilon_{\max}$ )
2:    $\boldsymbol{\psi}' \leftarrow \boldsymbol{\psi}$ 
3:   for  $q \in \{1, 2, \dots, Q\}$  do
4:      $\{\mathbf{w}_r, \mathbf{w}_t\} \leftarrow \text{ALTMIN}(\mathbf{A}, \boldsymbol{\psi}', 1, k_{\max}, \varepsilon_{\max})$ 
5:     for  $x \in \{t, r\}$  do
6:        $\{\mathbf{F}_{x,q}, \mathbf{c}_{x,q}\} \leftarrow \text{GREEDYSUB}(\mathbf{w}_x, M_x, B)$ 
7:        $\mathbf{F}_x \leftarrow [\mathbf{F}_{x,1}, \dots, \mathbf{F}_{x,q}]$ 
8:        $\{\mathbf{C}_t, k, \varepsilon\} \leftarrow \{[\mathbf{c}_{t,1}, \dots, \mathbf{c}_{t,q}], 0, \infty\}$ 
9:       while  $k < k_{\max} \wedge \varepsilon > \varepsilon_{\max}$  do ▷ alternating min.
10:        Update  $\mathbf{C}_r$  and  $\mathbf{C}_t$  using (19) and (20)
11:         $\boldsymbol{\psi}' \leftarrow \boldsymbol{\psi} - \mathbf{A}^T \text{vec}(\mathbf{F}_r(\mathbf{I} \odot \mathbf{C}_r)(\mathbf{I} \odot \mathbf{C}_t)^T \mathbf{F}_t^T)$ 
12:         $\{\varepsilon, k\} \leftarrow \{\|\boldsymbol{\psi}'\|_2^2, k + 1\}$ 
13:   return  $\mathbf{F}_r, \mathbf{F}_t, \mathbf{C}_r, \mathbf{C}_t$ 

```

(P5) is found using alternating minimization, which iterates between the following least squares solutions:

$$\mathbf{C}_r = \text{mat}_{M_r \times q}((\mathbf{A}^T((\mathbf{F}_t(\mathbf{I} \odot \mathbf{C}_t) \otimes \mathbf{1}_{M_r}^T) \odot \mathbf{F}_r))^{\dagger} \boldsymbol{\psi}) \quad (19)$$

$$\mathbf{C}_t = \text{mat}_{M_t \times q}((\mathbf{A}^T(\mathbf{F}_t \odot (\mathbf{F}_r(\mathbf{I} \odot \mathbf{C}_r) \otimes \mathbf{1}_{M_t}^T))^{\dagger} \boldsymbol{\psi}). \quad (20)$$

Algorithm 3 does not necessarily converge to the fully digital solution found by Algorithm 1, even as $B \rightarrow \infty$. This is because Algorithm 1 is called sequentially using a single component image (instead of Q) on line 4 of Algorithm 3. Consequently, when B is large, a better solution may be obtained by applying Algorithm 2 to the fully digital solution found by Algorithm 1 (provided $M \geq 2$). However, we will show in Section VII-B that Algorithm 3 produces better results in the interesting regime of small to moderate B (say, $B \leq 6$).

3) *Worst-case complexity:* The worst-case complexity of Algorithm 2 is dominated by the pseudo-inverse on line 6. Since the dimension of matrix $\mathbf{F}_{:,1:2m}$ changes at each iteration, the total complexity of Algorithm 2 is proportional to

$$\sum_{m=1}^{\lfloor M/2 \rfloor} N^2 m = \mathcal{O}(N^2 M^2).$$

The most expensive operations in Algorithm 3 are (i) calling Algorithm 1 on line 4; (ii) calling Algorithm 2 on line 6; (iii) evaluating the pseudo-inverses on line 10; and (iv) computing the matrix-vector product on line 11. Assuming again that $N_x \propto N$ and $M_x \propto M$, the complexity of (i) reduces to $\mathcal{O}(k_{\max}VNQ \max(V, N))$, or $\mathcal{O}(k_{\max}V^2NQ)$ if $V \geq N$. Furthermore, (ii) has complexity $\mathcal{O}(QN^2M^2)$. Denoting $m = \max(V, qM)$, $n = \min(V, qM)$, and $\varrho = \min(V/M, Q)$, the complexity of (iii) is proportional to

$$\begin{aligned} k_{\max} \sum_{q=1}^Q m^2 n &= k_{\max}VM \left(V \sum_{q=1}^{\lfloor \varrho \rfloor} q + M \sum_{q=\lfloor \varrho \rfloor+1}^Q q^2 \right) \\ &= \mathcal{O}(k_{\max}VM \max(V\varrho^2, M(Q^3 - \varrho^3))). \end{aligned}$$

This is upper bounded by $\mathcal{O}(k_{\max}VMQ^2 \max(V, MQ))$, since $\varrho \in [0, Q]$. Finally, the cost of (iv) is $\mathcal{O}(k_{\max}VN^2Q)$. Consequently, the worst-case complexity of Algorithm 3 is

$$\mathcal{O}(k_{\max}VQ \max(VN, VMQ, M^2Q^2) + N^2M^2Q).$$

As $V \propto N$ for a uniform array and $V \propto N^2$ for a sparse array, the complexity of Algorithm 3 is at most on the order of N^3 (uniform array) or N^5 (sparse array), and Q^3 (both).

C. Fully analog beamformer

Algorithms 2 and 3 are directly applicable to fully analog beamformer design by setting $M_x = 1$. We note that problems (P1) and (P2) also simplify significantly in the analog case. This was exploited in the companion paper [22] to develop a more efficient algorithm when $B \rightarrow \infty$. Investigations into improved fully analog beamforming algorithms for finite B are however beyond the scope of this paper.

D. Remarks on the computational complexity

We conclude this section with two remarks regarding the computational complexity of solving the optimization problems formulated in Section III.

Firstly, we may have to solve (P1) for several steering directions \mathbf{u} in practice. For example, if the number of phase shift bits B is small, the number of desired steering directions may be larger than that accommodated by the 2^B quantized phase shifts. Even if B is large, the PSF may not be translation invariant, as, for instance, when sensors have directive gain patterns or scatterers are located in the near field of the array.

TABLE III: Properties of closed-form beamformers proposed in Section VI.

Theorem	Beamforming architecture	# of front ends, M_x	# of phase shifters	# of phase shift bits, B	# of component images ^b Q
n/a	Digital	N_x	0	n/a	$\text{rank}(\mathbf{W})$
1	Hybrid	2	$2N_x$	∞	$\text{rank}(\mathbf{W})$
2	Hybrid	2	$2N_x$	1	$N_r N_t$
3	Analog	1	N_x	∞	$4\text{rank}(\mathbf{W})$
4	Analog	1	N_x	1	$4N_r N_t$
1 + Remark 1	Analog ^c	1	$2N_x$	∞	$\text{rank}(\mathbf{W})$
2 + Remark 1	Analog ^c	1	$2N_x$	1	$N_r N_t$

^b Note that $\text{rank}(\mathbf{W}) \leq \max(N_r, N_t)$.

^c Requires modification to the architecture in Fig. 1 (see Remark 1 in Section IV).

Secondly, sparsity can be leveraged to speed up computations. For example, (17)–(20) contain sparse matrices resulting from the Kronecker and Khatri-Rao products with the identity matrix. This can be exploited when computing the pseudo-inverse using, e.g., *power* or *orthogonal iterations* [25, pp. 366-368], especially if there are only a few dominant singular values. Furthermore, solving (P1) for a desired co-array weight vector in (12), instead of the PSF in (6) allows us to replace ψ by \mathbf{w}_Σ , \mathbf{A} by Υ^T , and V by N_Σ in Algorithms 1 and 3. The computational advantage follows from the fact that Υ is sparse with only $N_t N_r$ non-zero entries, which is a factor of V less than the $V N_t N_r$ entries of full matrix \mathbf{A} . The solutions obtained using Υ and \mathbf{A} are equivalent when the sum co-array steering matrix \mathbf{A}_Σ in (11) is a (scaled) unitary matrix. This is the case, e.g., when the columns of \mathbf{A} are sampled uniformly in $V = N_\Sigma$ unique directions, and the array elements are ideal and omnidirectional.

VI. BOUNDS ON THE NUMBER OF COMPONENT IMAGES Q

In this section, we derive closed-form solutions for $\mathbf{F}_{x,q}$, $\mathbf{c}_{x,q}$ assuming zero approximation error ($\epsilon_{\max} = 0$). These solutions then yield upper bounds on Q in problem (P1) for $M_x \in \{1, 2, N_x\}$ and $B \in \{1, \infty\}$. Each beamformer makes a different trade-off between the number of front ends M_x , phase shift bits B , and component images Q , as summarized in Table III. We find that for any number of phase shift bits B , the number of component images required by a hybrid beamformer satisfies $\text{rank}(\mathbf{W}) \leq Q \leq N_r N_t$, where $\text{rank}(\mathbf{W}) \leq \min(N_r, N_t)$ is the number of component images required by the fully digital beamformer. Similarly, for the fully analog beamformer we have $\text{rank}(\mathbf{W}) \leq Q \leq 4N_r N_t$.

A. Fully digital beamformer

In the case of fully digital beamforming, the SVD guarantees that any co-array weight matrix $\mathbf{W} \in \mathbb{C}^{N_r \times N_t}$ in (8) can be factorized using Q component images, where

$$Q = \text{rank}(\mathbf{W}) \leq \min(N_t, N_r). \quad (21)$$

We may also obtain a lower bound on Q by considering the number of degrees of freedom available for realizing a desired PSF. Specifically, assuming (11) holds, a simple comparison of the number of equations and unknowns in (12) yields the following necessary condition on Q .

Proposition 1 (Lower bound on Q). *Let $\mathbf{W} \in \mathbb{C}^{N_r \times N_t}$ be a rank- Q matrix. Then (12) holds for any $\mathbf{w}_\Sigma \in \mathbb{C}^{N_\Sigma}$ only if*

$$Q \geq \frac{N_t + N_r - \sqrt{(N_t + N_r)^2 - 4N_\Sigma}}{2}. \quad (22)$$

Proof. In (12), the number of equations is $N_\Sigma \leq N_t N_r$, and the number of free variables is $Q(N_t + N_r - Q)$, since \mathbf{W} is a rank- Q matrix. A necessary condition for (12) to hold for any $\mathbf{w}_\Sigma \in \mathbb{C}^{N_\Sigma}$ is therefore that $Q(N_t + N_r - Q) \geq N_\Sigma$. This quadratic inequality directly yields the bound in (22). \square

Eq. (22) is a necessary lower bound on Q only when (12) is required to hold for any co-array beamforming weight vector $\mathbf{w}_\Sigma \in \mathbb{C}^{N_\Sigma}$. For a fixed \mathbf{w}_Σ , a rank- Q matrix \mathbf{W} may exist that satisfies (12) but not (22).

It is instructive to evaluate (22) for some typical array configurations. Firstly, if the array is non-redundant, every Tx-Rx pair uniquely maps to one sum co-array element, which implies that $N_\Sigma = N_t N_r$. Consequently, (22) reduces $Q \geq \min(N_t, N_r)$, which together with (21) yields

$$Q = \min(N_t, N_r).$$

Secondly, if the transceivers are co-located, we have $N_x = N$, and (22) simplifies to

$$Q \geq N - \sqrt{N^2 - N_\Sigma}. \quad (23)$$

For example, the *uniform linear array* has $N_\Sigma = 2N - 1$, which yields $Q \geq 1$. Consequently, a single component image may suffice to achieve any PSF supported on the sum co-array of this array. Similar results can be shown to hold for higher dimensional uniform arrays, such as the *uniform rectangular array*. In contrast, (23) scales linearly with N for sparse arrays, since $N_\Sigma \propto \zeta N^2$, with $0 < \zeta < 1$. This leads to the inequality $Q \gtrsim N(1 - \sqrt{1 - \zeta})$ that holds approximately

for large N . In practice, the linear dependence between N and Q is weak. For instance, the square *boundary array* [2] with $\zeta = 1/4$ yields the bound $Q \gtrsim N(2 - \sqrt{3})/2 > 0.13N$. The greatest lower bound in (23) is given by the array configuration maximizing N_Σ given N . This is the *minimum-redundancy array* [26]–[29], if the sum co-array is required to be uniform.

B. Hybrid beamformer

It is not evident for which values of Q, M and B factorization (9) is feasible, given a general co-array weight matrix $\mathbf{W} \in \mathbb{C}^{N_r \times N_t}$. Next, we show that $M_x = 2$ Tx/Rx front ends are sufficient for feasibility, irrespective of the number of phase shifter bits B .

1) *Continuous phase shifters*: Lemma 1 implies that (9) provides a feasible factorization when $Q = \text{rank}(\mathbf{W})$, provided $M_x = 2$ and $B \rightarrow \infty$. In this case, the hybrid beamforming weights are given by the following theorem:

Theorem 1 (Hybrid beamformer, continuous phase shifters, two Tx/Rx front ends). *Let $M_x = 2$ and $B \rightarrow \infty$. Any $\mathbf{W} = \sum_{q=1}^Q \mathbf{w}_{r,q} \mathbf{w}_{t,q}^T \in \mathbb{C}^{N_r \times N_t}$ may be factorized as $\mathbf{W} = \sum_{q=1}^Q \mathbf{F}_{r,q} \mathbf{c}_{r,q} \mathbf{c}_{t,q}^T \mathbf{F}_{t,q}^T$, with $\mathbf{c}_{x,q} \in \mathbb{C}^2$; and $\mathbf{F}_{x,q} \in \mathcal{F}_x(\infty)$ following (3). For example, a valid factorization is*

$$\mathbf{F}_{x,q} = \exp \left(j \left(\angle \mathbf{w}_{x,q} \mathbf{1}_2^T + \cos^{-1} \left(\frac{|\mathbf{w}_{x,q}|}{\|\mathbf{w}_{x,q}\|_\infty} \right) (\mathbf{1}_2 - 2\mathbf{e}_2)^T \right) \right) \quad (24)$$

$$\mathbf{c}_{x,q} = \frac{\|\mathbf{w}_{x,q}\|_\infty}{2} \mathbf{1}_2. \quad (25)$$

Here $\mathbf{1}_2$ is a vector of ones, \mathbf{e}_2 is the standard unit vector, and \angle , \cos^{-1} , and $|\cdot|$ are applied elementwise.

Proof. This follows directly from Lemma 1, since each $\mathbf{w}_{x,q}$ can be factorized as $\mathbf{w}_{x,q} = \mathbf{F}_{x,q} \mathbf{c}_{x,q}$. \square

Note that the factorization in Theorem 1 is not unique, and more general expressions for $\mathbf{F}_{x,q}$ and $\mathbf{c}_{x,q}$ are easily obtained (see Lemma 1 in Section IV and the proof in Appendix A).

2) *One-bit phase shifters*: The phases of the phase shifters may be coarsely quantized in practice [11]. In this case, Theorem 1 no longer holds even approximately. However, any co-array weight matrix $\mathbf{W} \in \mathbb{C}^{N_r \times N_t}$ can still be achieved using only two Tx/Rx front ends and one-bit phase quantization. This is accomplished at the expense of increasing the number of component images to $Q = N_r N_t \gg \min(N_r, N_t) \geq \text{rank}(\mathbf{W})$. The hybrid weight matrices in (9) are again obtained in closed form, as shown by the following theorem.

Theorem 2 (Hybrid beamformer, 1-bit phase shifters, two Tx/Rx front ends). *Let $M_x = 2$ and $B = 1$. Any $\mathbf{W} \in \mathbb{C}^{N_r \times N_t}$ may be factorized as $\mathbf{W} = \sum_{q=1}^{N_r N_t} \mathbf{F}_{r,q} \mathbf{c}_{r,q} \mathbf{c}_{t,q}^T \mathbf{F}_{t,q}^T$ with $\mathbf{c}_{r,q}, \mathbf{c}_{t,q} \in \mathbb{C}^2$, and $\mathbf{F}_{x,q} \in \mathcal{F}_x(1)$ following (3). For example, a valid factorization is*

$$\mathbf{F}_{x,q} = [\mathbf{1}_{N_x}, 2\mathbf{e}_{n_x} - \mathbf{1}_{N_x}] \quad (26)$$

$$\mathbf{c}_{x,q} = \frac{\sqrt{W_{n_r n_t}}}{2} \mathbf{1}_2, \quad (27)$$

where $n_r = 1 + (q-1) \bmod N_r$ and $n_t = \lceil q/N_r \rceil$.

Proof. Eq. (26) ensures that each of the $Q = N_r N_t$ terms in (9) contribute to exactly one entry of matrix $\mathbf{W} \in \mathbb{C}^{N_r \times N_t}$. In particular, substituting (26) and $c_{x,q} \mathbf{1}_2$ into (9) yields $\mathbf{F}_{x,q} \mathbf{c}_{x,q} = 2c_{x,q} \mathbf{e}_{n_x}$, where $\mathbf{e}_{n_x} \in \{0, 1\}^{N_x}$ is the standard unit vector of length N_x with a unit entry at index $n_x \in \{1, 2, \dots, N_x\}$. Consequently, the q th term in (9) becomes

$$\mathbf{F}_{r,q} \mathbf{c}_{r,q} \mathbf{c}_{t,q}^T \mathbf{F}_{t,q}^T = 4c_{r,q} c_{t,q} \mathbf{e}_{n_r} \mathbf{e}_{n_t}^T,$$

where $q = n_r + (n_t - 1)N_r$. If $4c_{r,q} c_{t,q} = W_{n_r n_t}$ then, as desired,

$$\sum_{q=1}^{N_r N_t} \mathbf{F}_{r,q} \mathbf{c}_{r,q} \mathbf{c}_{t,q}^T \mathbf{F}_{t,q}^T = \sum_{n_r=1}^{N_r} \sum_{n_t=1}^{N_t} \mathbf{e}_{n_r} \mathbf{e}_{n_t}^T W_{n_r n_t} = \mathbf{W}.$$

Choosing $c_{r,q} = c_{t,q} = \sqrt{W_{n_r n_t}}/2$ then yields (27). \square

Theorem 2 implies that the hybrid beamformer with at least two Tx/Rx front ends can achieve the PSF of the fully digital beamformer, regardless of the number of bits used to quantize the phase shifters. This is facilitated by image addition, which trades off an increase in the number of component images Q for lower quantization precision B , and fewer Tx/Rx front ends M_x . As a corollary of Theorem 2, we see that the number of component images of the hybrid beamformer is always upper bounded by $Q \leq N_r N_t$, since a trivial solution with $M_x \geq 2$; $Q = N_r N_t$; $B \geq 1$ is achieved by appending columns with arbitrary phases to (26), and zeros to (27).

C. Fully analog beamformer

A fully analog beamformer may be constructed directly from a hybrid architecture by either increasing the number of component images Q , or by modifying the beamforming architecture as in Remark 1 of Section IV. In the latter case, the number of phase shifters is still $M_x N_x$, although only a single Tx/Rx front end is used. Actually, the number of phase shifters can be reduced to half by doubling Q . More generally, the following lemma shows that the total number

of phase shifters can be reduced from $M_t N_t + M_r N_r$ to $N_t + N_r$ by increasing the number of component images from Q to $M_t M_r Q$.

Lemma 3 (Analog beamforming weights from hybrid beamforming weights). *Any $\mathbf{W} = \sum_{\tilde{q}=1}^Q \mathbf{F}_{r,\tilde{q}} \mathbf{c}_{r,\tilde{q}} \mathbf{c}_{t,\tilde{q}}^T \mathbf{F}_{t,\tilde{q}}^T \in \mathbb{C}^{N_r \times N_t}$, where $\mathbf{F}_{x,\tilde{q}} \in \mathbb{C}^{N_x \times M_x}$ and $\mathbf{c}_{x,\tilde{q}} \in \mathbb{C}^{M_x}$, can be factorized as $\mathbf{W} = \sum_{q=1}^{M_r M_t Q} c_{r,q} c_{t,q} \mathbf{f}_{r,q} \mathbf{f}_{t,q}^T$. For example, a valid choice is*

$$\mathbf{f}_{x,q} = [\mathbf{F}_{x,\lceil q/(M_r M_t) \rceil}]_{:,m_x} \quad (28)$$

$$c_{x,q} = [\mathbf{c}_{x,\lceil q/(M_r M_t) \rceil}]_{m_x}, \quad (29)$$

where $m_r = \lceil (1 + (q - 1) \bmod M_r M_t) / M_t \rceil$ and $m_t = 1 + (q - 1) \bmod M_t$.

Proof. See Appendix C.

1) *Continuous phase shifters:* Recall from Theorem 1 that a hybrid beamformer with continuous phase shifters can achieve any fully digital beamforming vectors using only two Tx/Rx front ends. By Lemma 3, the number of front ends may further be halved by quadrupling the number of component images Q , as shown by the following theorem (cf. [22, Theorem 1]).

Theorem 3 (Analog beamformer, continuous phase shifters). *Let $M_x = 1$ and $B \rightarrow \infty$. Any $\mathbf{W} = \sum_{\tilde{q}=1}^Q \mathbf{w}_{r,\tilde{q}} \mathbf{w}_{t,\tilde{q}}^T \in \mathbb{C}^{N_r \times N_t}$ may be factorized as $\mathbf{W} = \sum_{q=1}^{4Q} c_{r,q} c_{t,q} \mathbf{f}_{r,q} \mathbf{f}_{t,q}^T$, with $c_{x,q} \in \mathbb{C}$; and $\mathbf{f}_{x,q} \in \mathcal{F}_x(\infty)$ following (3). For example, a valid factorization is*

$$\mathbf{f}_{x,q} = \exp \left(j \left(\angle \mathbf{w}_{x,\tilde{q}} + (-1)^{i_x+1} \cos^{-1} \left(\frac{|\mathbf{w}_{x,\tilde{q}}|}{\|\mathbf{w}_{x,\tilde{q}}\|_\infty} \right) \right) \right) \quad (30)$$

$$c_{x,q} = \|\mathbf{w}_{x,\tilde{q}}\|_\infty / 2, \quad (31)$$

where $\tilde{q} = \lceil q/4 \rceil$; $i_r = \lceil (1 + (q - 1) \bmod 4) / 2 \rceil$; and $i_t = 1 + (q - 1) \bmod 2$.

Proof. By Theorem 1, we have

$$\mathbf{W} = \sum_{\tilde{q}=1}^Q \mathbf{w}_{r,\tilde{q}} \mathbf{w}_{t,\tilde{q}}^T = \sum_{\tilde{q}=1}^Q \mathbf{F}_{r,\tilde{q}} \mathbf{c}_{r,\tilde{q}} \mathbf{c}_{t,\tilde{q}}^T \mathbf{F}_{t,\tilde{q}}^T,$$

where $\mathbf{F}_{x,\tilde{q}} \in \mathcal{F}_x(\infty) \subset \mathbb{C}^{N_x \times 2}$ and $\mathbf{c}_{x,\tilde{q}} \in \mathbb{C}^2$. Factorization into analog beamforming weights using Lemma 3 then yields

$$\mathbf{W} = \sum_{\tilde{q}=1}^Q \sum_{i=1}^2 \sum_{l=1}^2 [c_{r,\tilde{q}}]_i [c_{t,\tilde{q}}]_l [\mathbf{F}_{r,\tilde{q}}]_{:,i} [\mathbf{F}_{t,\tilde{q}}]_{:,l}^T = \sum_{q=1}^{4Q} c_{r,q} c_{t,q} \mathbf{f}_{r,q} \mathbf{f}_{t,q}^T.$$

Substituting (24) and (25) into this expression, and properly accounting for the summation indices yields (30) and (31). \square

2) *One-bit phase shifters*: According to Remark 1 in Section IV, we may reduce the number of Tx/Rx front ends in Theorem 2 to one, since the digital weight vector in (27) is a scaled unit vector. Similarly to Theorem 3, the number of phase shifters may further be reduced to half.

Theorem 4 (Analog beamformer, 1-bit phase shifters). *Let $M_x = 1$ and $B = 1$. Any $\mathbf{W} \in \mathbb{C}^{N_r \times N_t}$ may be factorized as $\mathbf{W} = \sum_{q=1}^{4N_r N_t} c_{r,q} c_{t,q} \mathbf{f}_{r,q} \mathbf{f}_{t,q}^T$, with $c_{x,q} \in \mathbb{C}$, and $\mathbf{f}_{x,q} \in \mathcal{F}_x(1)$ following (3). For example, a valid factorization is*

$$\mathbf{f}_{x,q} = (\mathbf{e}_{n_x} - \mathbf{1}_{N_x})(-1)^{i_x} + \mathbf{e}_{n_x} \quad (32)$$

$$c_{x,q} = \sqrt{W_{n_r n_t}}/2, \quad (33)$$

where $i_r = \lceil (1 + (q-1) \bmod 4)/2 \rceil$; $i_t = 1 + (q-1) \bmod 2$; $n_r = 1 + (\lceil q/4 \rceil - 1) \bmod N_r$; and $n_t = \lceil q/(4N_r) \rceil$.

Proof. By Theorem 2 and Lemma 3, we have

$$\mathbf{W} = \sum_{\tilde{q}=1}^{N_r N_t} \mathbf{F}_{r,\tilde{q}} \mathbf{c}_{r,\tilde{q}} \mathbf{c}_{t,\tilde{q}}^T \mathbf{F}_{t,\tilde{q}}^T = \sum_{q=1}^{4N_r N_t} c_{r,q} c_{t,q} \mathbf{f}_{r,q} \mathbf{f}_{t,q}^T,$$

where $\mathbf{F}_{x,\tilde{q}} \in \mathcal{F}_x(1) \subset \mathbb{C}^{N_x \times 2}$; $\mathbf{c}_{x,\tilde{q}} \in \mathbb{C}^2$; $\mathbf{f}_{x,q} \in \mathcal{F}_x(1) \subset \mathbb{C}^{N_x}$; and $c_{x,q} \in \mathbb{C}$ (cf. Theorem 2). Equations (32) and (33) then follow from (26), (27), and the indexing in Lemma 3. \square

A direct corollary of Theorem 4 is that the number of component images of the analog beamformer is upper bounded by $Q \leq 4N_r N_t$, since $\mathcal{F}_x(1) \subseteq \mathcal{F}_x(B \geq 1)$. The bound is not necessarily tight, as the gap between the bounds presented in this section and the solutions found by Algorithm 3 can be significant, as we will show in the next section. Establishing tighter bounds is therefore an important topic for future work.

VII. NUMERICAL EXPERIMENTS

This section presents numerical results using the beamforming weight optimization algorithms developed in Section V and the closed-form beamformer designs derived in Section VI. We first introduce the necessary preliminaries and describe the simulation setup. We then evaluate the performance of Algorithm 1 and 3 for randomly drawn target PSFs, and study how trade-offs among the main parameters M , B , and Q affect the realized PSF. Lastly, we simulate a planar array imaging far-field scatterers. We show that a sparse hybrid array with coarsely quantized phase shifters can achieve comparable image quality to a fully digital uniform array.

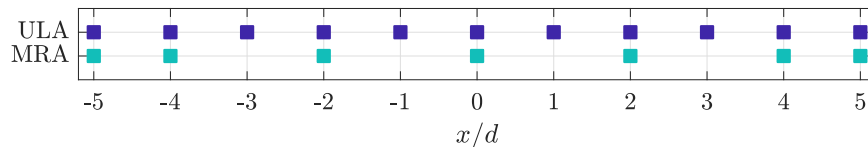


Fig. 4: Linear array configurations (co-located transceivers). The MRA with $N = 7$ elements is (sum) co-array equivalent to the ULA with $N = 11$ elements.

A. Preliminaries and simulation setup

1) *Linear array model:* The linear array is a useful model for illustrating the impact of different design parameters in a simple and intuitive manner. Consequently, in Sections VII-B to VII-D, we consider two linear array configurations with co-located transceivers: the *uniform linear array* (ULA), and the *minimum-redundancy array* (MRA) [26], [27]. The MRA has the largest uniform sum co-array for a given number of elements. Since each sensor is used for both transmission and reception, we denote $N = N_x$ and $M = M_x$. We assume that the elements are identical and omnidirectional with a unit inter-element spacing of half a wavelength ($d = \lambda/2$). No mutual coupling between the elements is considered. We particularly study the $N = 11$ element ULA, and $N = 7$ element MRA in more detail (Fig. 4). The two arrays span the same aperture 5λ and are sum co-array equivalent. The Tx and Rx steering vectors of the arrays are given by $\mathbf{a} = \mathbf{a}_t = \mathbf{a}_r$, where

$$\mathbf{a}(\varphi) = \exp(j\pi \mathbf{d} \sin \varphi).$$

Here, $\mathbf{d} \in \mathbb{Z}^N$ denotes the element positions on the x -axis normalized by $\lambda/2$. For the ULA $\mathbf{d} = [-5, -4, \dots, 5]^T$, and for the MRA $\mathbf{d} = [-5, -4, -2, 0, 2, 4, 5]^T$. A complete list of MRAs with $N \leq 42$ elements can be found in [28].

2) *Planar array model:* Planar arrays are often used in active sensing and imaging applications. Consequently, in Section VII-E, we consider the square uniform rectangular array (URA) and boundary array (BA) [2] shown in Fig. 5. Both arrays have a side length of 16 unit inter-element spacings and an equivalent uniform sum co-array. The unit distance between elements is set to $d = \lambda/2$, and the number of elements is $N = 289$ in the case of the URA, and $N = 64$ in case of the BA. All elements are used for both transmission and reception, which means that the fully digital beamforming architecture requires N ADCs/DACs. The BA in Fig. 5 (b) also satisfies the minimum-redundancy property, which implies that it has the fewest elements of all

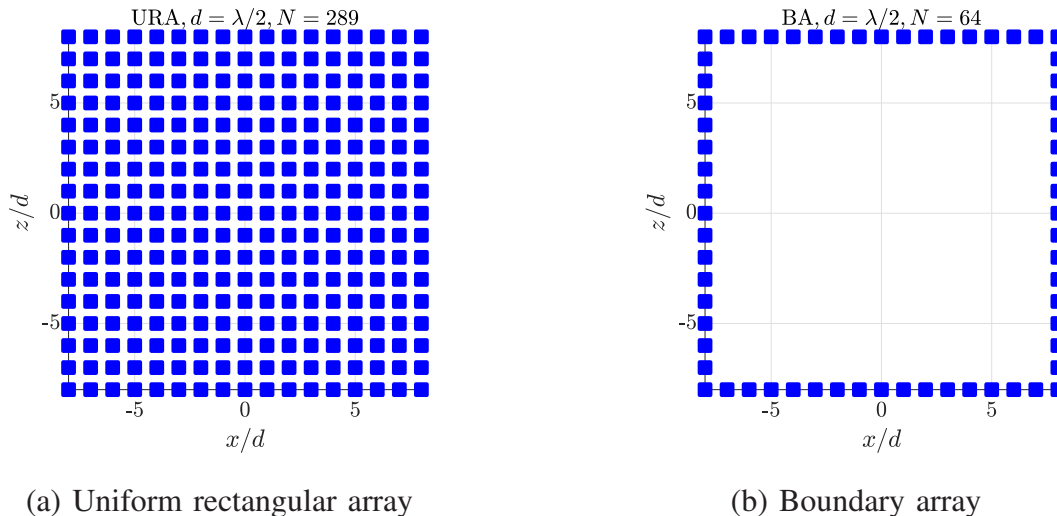


Fig. 5: Planar square arrays (co-located transceivers). The two arrays are co-array equivalent, although the BA in (b) uses almost 78% fewer physical elements than the URA in (a).

arrays that are sum co-array equivalent with the URA in Fig. 5 (a) [29]. Note that other sparse array configurations with this property also exist [30].

We ignore mutual coupling and assume that the array elements have identical sinusoidal gain patterns $g(\varphi, \theta) = \cos \varphi \sin \theta$. Consequently, the (transmit and receive) steering vectors assume the form

$$\mathbf{a}(\varphi, \theta) = \cos \varphi \sin \theta \exp(j\pi(\mathbf{d}_x \sin \varphi \sin \theta + \mathbf{d}_z \cos \theta)),$$

where $\mathbf{d}_x \in \mathbb{Z}^N$ and $\mathbf{d}_z \in \mathbb{Z}^N$ are the x and z coordinates of the elements normalized by $\lambda/2$, as illustrated in Fig. 5.

3) *Stochastic PSF model*: For performance evaluation purposes, we generate the desired co-array weight vector \mathbf{w}_Σ randomly from a uniform distribution (within the complex unit sphere). Specifically, the i th entry of the vector \mathbf{w}_Σ becomes

$$[\mathbf{w}_\Sigma]_i = \sqrt{r_i} e^{j\phi_i}, \text{ where } r_i \sim \mathcal{U}(0, 1) \text{ and } \phi_i \sim \mathcal{U}(0, 2\pi).$$

Using this model, we may conveniently sample the parameter space of feasible PSFs uniformly at random in Section VII-B.

4) *Deterministic PSF model*: From the application point of view, the stochastic model in Section VII-A3 may not generate interesting PSFs that have a narrow main lobe and low side lobe levels. We therefore also consider four deterministic PSFs that are commonly used in

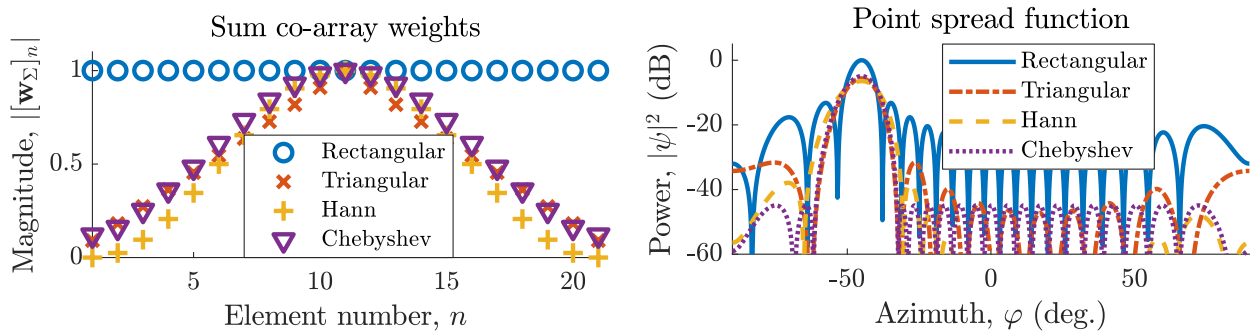


Fig. 6: Typical sum co-array beamforming weights (left) and corresponding PSFs (right) of the arrays in Fig. 4 (steering direction $\varphi = -45^\circ$). Each PSF makes a different trade-off among the main lobe width, array gain, and side-lobe levels.

beamforming [1] and power spectrum estimation [31]. Fig. 6 shows the magnitudes of the rectangular, triangular, Hann, and Dolph-Chebyshev [32] beamforming weights \mathbf{w}_Σ and the corresponding PSFs ψ .

5) *Algorithm parameters and performance criterion:* In order to speed up computations, we solve (P2) for a desired co-array beamforming weight vector $\mathbf{w}_\Sigma \in \mathbb{C}^{N_\Sigma}$ instead of the sampled PSF $\psi \in \mathbb{C}^V$ (see Section V-D). We set the maximum number of iterations in Algorithm 1 to $k_{\max} = 100$, and to $k_{\max} = 10$ in Algorithm 3. We use an approximation error tolerance of $\varepsilon_{\max} = 10^{-16} \|\mathbf{w}_\Sigma\|_2^2$, except for Section VII-E, where we use $\varepsilon_{\max} = 10^{-6} \|\mathbf{w}_\Sigma\|_2^2$. Our performance criterion of choice is the *relative approximation error*

$$\epsilon = \|\mathbf{w}_\Sigma - \Upsilon \text{vec}(\mathbf{W})\|_2 / \|\mathbf{w}_\Sigma\|_2.$$

For an ensemble of realizations of ϵ , we evaluate the sample mean, or alternatively the median and 90% confidence interval (5% and 95% percentiles) of the sample.

6) *Computation of pseudo-inverse:* For numerical stability, we compute the (approximate) pseudo-inverse of a matrix \mathbf{X} using diagonal loading (ridge regression) as

$$(\mathbf{X})_\alpha^\dagger = (\mathbf{X}^H \mathbf{X} + \alpha \mathbf{I})^{-1} \mathbf{X}^H, \quad (34)$$

where $(\mathbf{X})_\alpha^\dagger \approx \mathbf{X}^\dagger$ holds for small values of the diagonal loading parameter $\alpha > 0$. Heuristics, such as regularization or truncated SVD, are often employed when $\mathbf{X}^H \mathbf{X}$ is ill-conditioned. We choose the value of α by trial-and-error, since determining a rigorous selection rule is out of scope of this paper. We generally set $\alpha = 10^{-9}$, with the exception of Section VII-E, where we use $\alpha = 10^{-4}$.

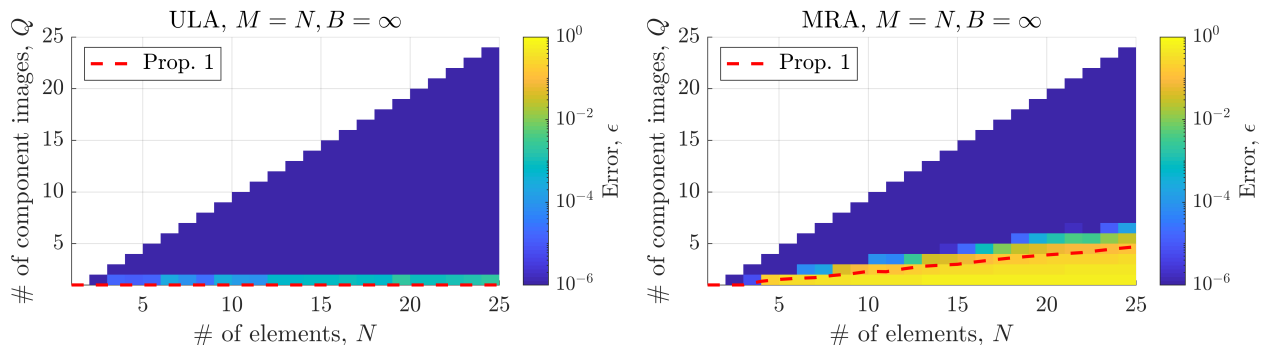


Fig. 7: Mean error of fully digital ULA (left) and MRA (right) beamformers (Algorithm 1). The error shows a phase transition approximately following the lower bound on Q in (22). This empirically validates the efficiency of Algorithm 1.

B. Validation of beamforming algorithms

In the following, we evaluate the two main algorithms, Algorithm 1 and 3, for 100 random i.i.d. realizations of the desired co-array weight vector \mathbf{w}_Σ following the stochastic model in Section VII-A3.

1) *Algorithm 1 (alternating minimization)*: Fig. 7 shows the mean relative approximation error of the fully digital beamforming weights found by Algorithm 1 as a function of the number of array elements N and component images Q . The lower bound on Q in (22) is also shown in red (dashed line). For the ULA, this bound is constant (equal to one), and for the MRA it has a weak linear dependence on N , since the MRA has larger sum co-array than the ULA for given N (see Section VI-A). We observe in both cases that a *phase transition*, where the error drops rapidly, coincides with the lower bound in (22). This empirically validates Algorithm 1.

Note that by Theorem 1, Fig. 7 also applies to the hybrid beamformer with continuous phase shifters ($B \rightarrow \infty$) and at least two Tx-Rx front-ends ($M = 2$). By Theorem 3, a fully analog beamformer with continuous phase shifters ($M = 1$ and $B \rightarrow \infty$) would achieve the same error level as the fully digital beamformers in Fig. 7 using at most four times as many component images.

2) *Algorithm 3 (greedy method)*: Fig. 8 shows the mean error of the hybrid beamforming weights found by Algorithm 3. The number of Tx/Rx front-ends is $M = 2$, and the number of phase shift bits is $B = 5$ (top row) and $B = 1$ (bottom row). The quantization of the phase shifts degrades the quality of the solution compared to the fully digital beamformer shown in

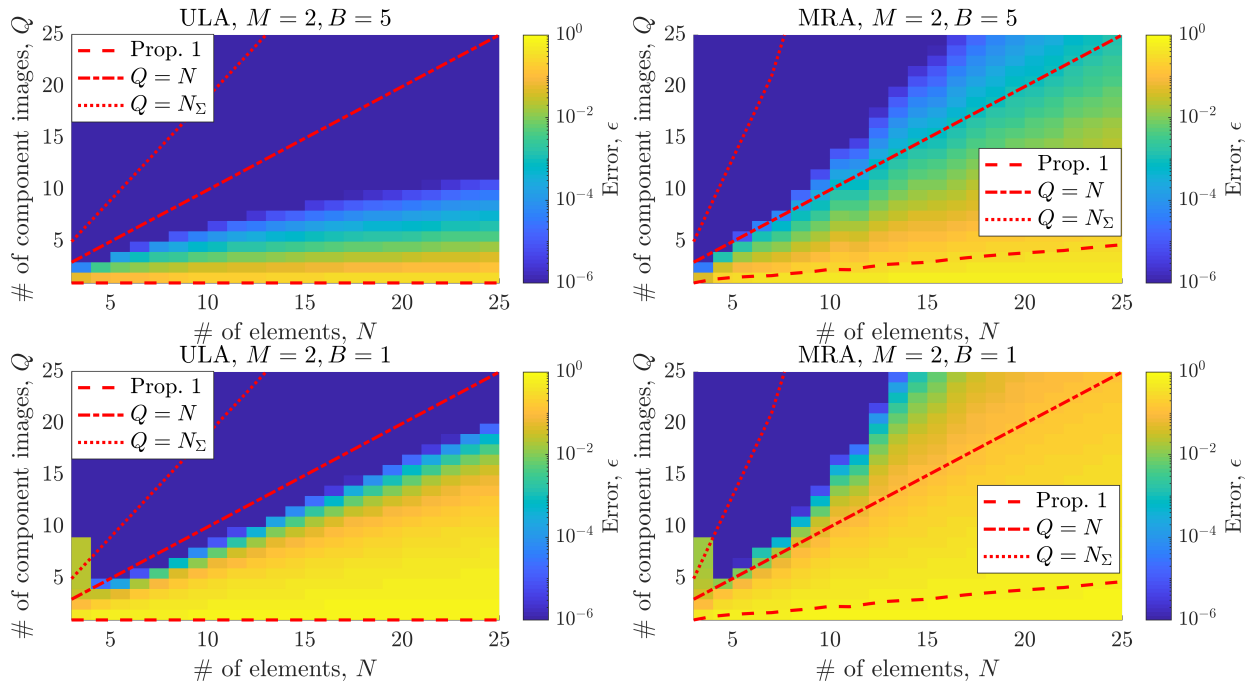


Fig. 8: Mean error of hybrid ULA (left) and MRA (right) beamformers with $M=2$ Tx/Rx front-ends, and $B=5$ (top) and $B=1$ (bottom) phase shift bits (Algorithm 3). The phase transition occurs for $Q < N_\Sigma$ even in the one bit case.

Fig. 7. However, even in the one bit case, the phase transition boundary of the error is far below the upper bound $Q \leq N^2$ suggested by Theorem 2. In fact, the phase transition obeys a tighter bound $Q < N_\Sigma$ (dotted line), where $N_\Sigma \leq N^2$ is the number of co-array elements. These findings suggest the possibility of both algorithmic improvements and tighter bounds in future work.

Fig. 9 shows the median error and 90% confidence intervals as a function of B and Q for the $N = 11$ element ULA and $N = 7$ element MRA. For the ULA (left), the error decreases rapidly as B increases up to approximately $B = 8$. After this, we see diminishing returns in increasing B . For the MRA (right), increasing B beyond $B = 6$ leads to little or no improvement in the error. This point of diminishing returns is lower than for the ULA, since the MRA has fewer elements.

A better solution may sometimes be obtained by quantizing the phase shifts of the beamformer provided by Theorem 1. Unlike Algorithm 3, this solution converges to that of Algorithm 1 (the fully digital beamformer) when $B \rightarrow \infty$, provided $M \geq 2$. However, the solution does not improve by increasing Q or M . As shown in Fig. 9, Algorithm 3 (colorful non-solid lines)

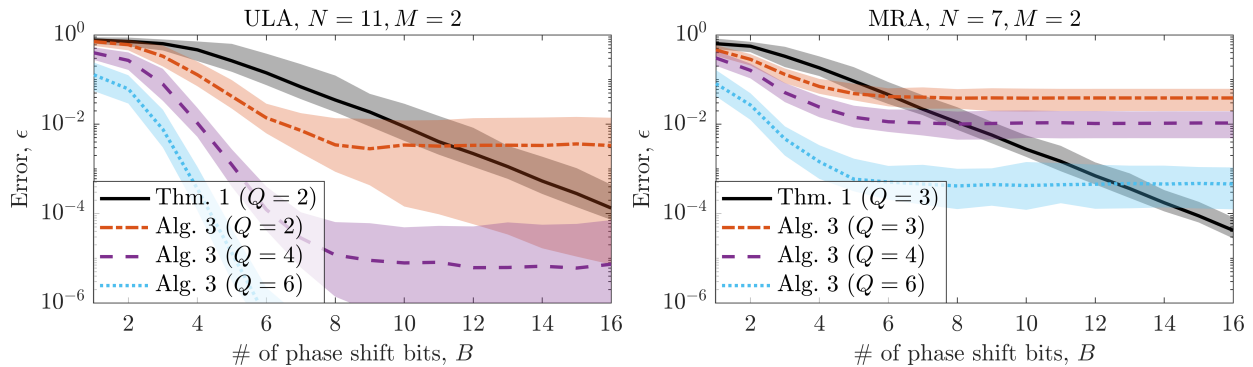


Fig. 9: Median error and 90% confidence intervals of hybrid ULA (left) and MRA (right) beamformers (two Tx/Rx front-ends). Algorithm 3 experiences diminishing returns in B , but achieves a lower median error than directly quantizing Theorem 1, when $B \leq 11$ (ULA) or $B \leq 6$ (MRA).

achieves a lower median error than directly quantizing Theorem 1 (black solid line³), for example, when $B \leq 11$ and $Q = 2$ in case of the ULA (left), or $B \leq 6$ and $Q = 3$ in case of the MRA (right). Even in the worst case, based on the 90% confidence intervals (shaded area), Algorithm 3 mostly yields a better solution when $B \leq 8$ (ULA) or $B \leq 4$ (MRA). This cross-over point shifts to higher values of B as the number of component images Q increases.

C. Point spread function of linear arrays

We now qualitatively study the point spread function of the arrays in Fig. 4 as a function of B and Q . For simplicity, we limit ourselves to the Dolph-Chebyshev beampattern in Fig. 6.

Fig. 10 shows the realized PSF of the hybrid ULA (left column) and MRA (right column) with $M = 2$ Tx/Rx front ends for $Q = 1$ (top row), $Q = 2$ (bottom row), and $B \in \{1, 5, \infty\}$. When $B \rightarrow \infty$, the ULA achieves the desired PSF using $Q = 1$ component image by application of Theorem 1 to the fully digital solution found by Algorithm 1. The sparser MRA requires $Q = 2$ for the same result. When B is finite, Algorithm 3 needs to be employed. The elevated sidelobes of the PSFs are reduced by increasing either B or Q .

Fig. 11 shows the realized PSF of the fully analog ($M = 1$) ULA (left column) and MRA (right column) for $Q = 4$ (top row), $Q = 8$ (bottom row), and $B \in \{1, 5, \infty\}$. Increasing Q

³We use the fully digital solution found by Algorithm 1 ($Q = 2$), and recompute the digital weight matrices \mathbf{C}_x using alternating minimization as on line 10 of Algorithm 3 with $k_{\max} = 100$ iterations.

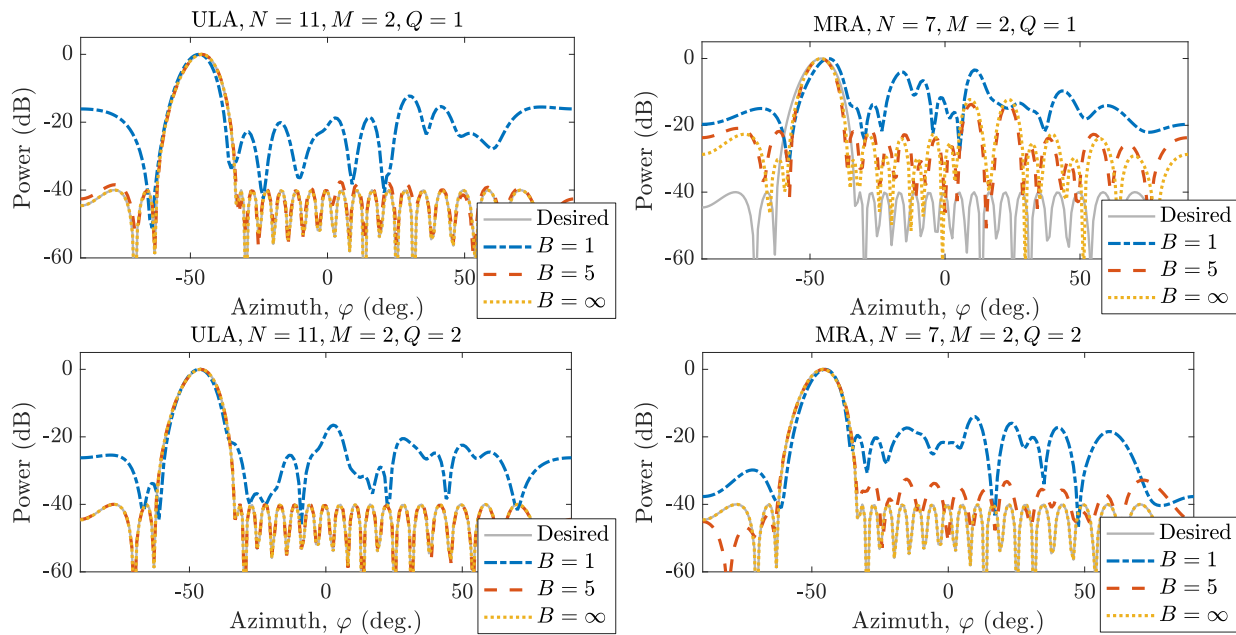


Fig. 10: PSF of hybrid ULA (left) and MRA (right) beamformers (two Tx/Rx front ends). The PSF improves when increasing the number of component images Q , or phase shift bits B .

decreases the mismatch between the desired and realized PSFs also in the analog case, although the rate of improvement is slower, and more component image are required compared to the hybrid case (cf. Fig. 10). When $B \rightarrow \infty$, the ULA and MRA achieve the desired PSF using $Q = 4$, respectively, $Q = 8$ component images by application of Theorem 3.

D. Trade-offs among main parameters M , Q and B

Next, we study the trade-offs among the three main design parameters M , Q , and B . We fix the number of quantization bits B and evaluate the relative approximation error against the number of component images Q for different numbers of Tx/Rx front ends M . We consider the linear arrays in Fig. 4 and the deterministic PSFs in Section VII-A4. Each PSF is steered in 100 different scan directions uniformly sampling the interval $[-\pi/2, \pi/2]$.

Fig. 12 shows the median error and 90% confidence intervals of the ULA (left column) and MRA (right column) as function of Q for $B = 1$ (top row), $B = 5$ (middle row), and $B \rightarrow \infty$ (bottom row). The number of Tx/Rx front ends M has a significant impact on the approximation error of the solution found by Algorithm 3. When $M = 1$ (fully analog case), the error decreases at a slower rate as a function of B and Q . When $M \geq 2$ and $B \rightarrow \infty$, the error drops abruptly,

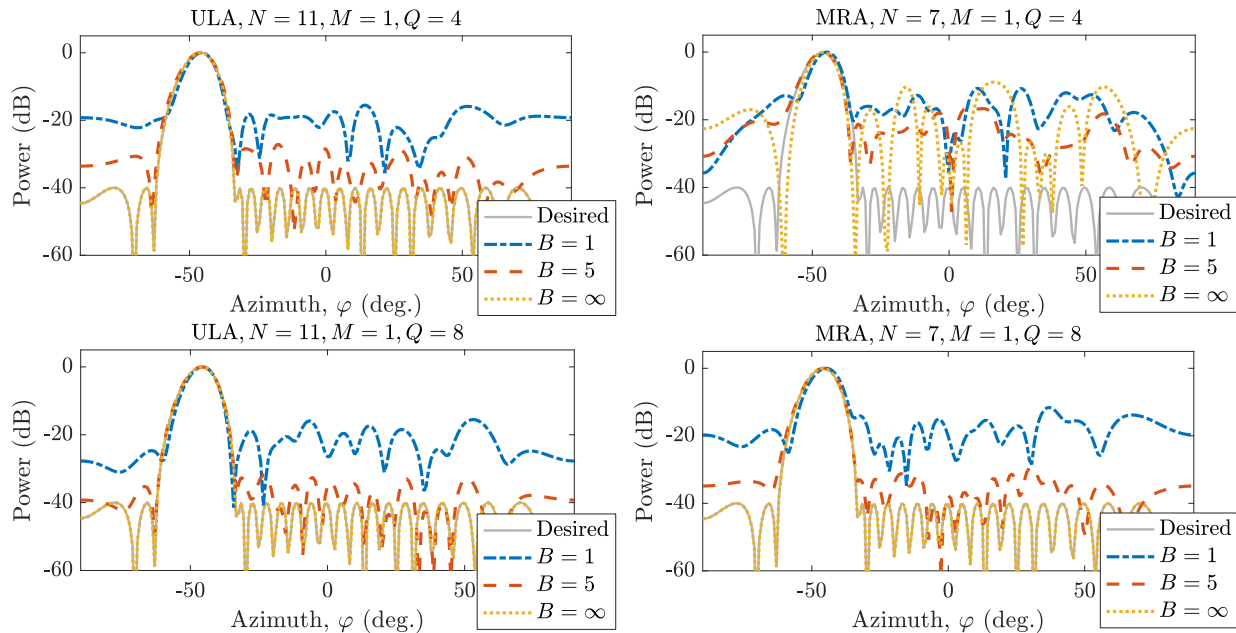


Fig. 11: PSF of fully analog ULA (left) and MRA (right) beamformers (one Tx/Rx front end). A high-fidelity PSF requires more component images than in the hybrid case.

since Theorem 1 can be applied to achieve the PSF of the fully digital beamformer using the same number of component images. By Theorem 3, the fully analog beamformer requires four times as many component images as the fully digital beamformer. Consequently, the discontinuities for $M=1, B \rightarrow \infty$ occur when $Q=4, 8, 12, 16$, etc.

Fig. 12 suggests that M and Q have a larger impact on the realized PSF than B . This is not surprising, since M and Q control the dimensions of \mathbf{F}_x and \mathbf{C}_x in (9), whereas B only adjusts the quantization of \mathbf{F}_x . In other words, B does not affect the number of phase shifters and digital weights, unlike M and Q . When B is finite, it is difficult to establish whether increasing M or Q will generally have a larger impact on the error of the realized PSF. However, when B is infinite, Q is practically the only free parameter, because $M=2$ suffices to achieve any fully digital factorization of \mathbf{W} by Theorem 1.

E. Coherent imaging with planar arrays

Fig. 13 shows the scattering scene imaged by the two sum co-array equivalent planar array configurations in Section VII-A2. The continuous rough surfaces of the reflecting objects are modeled by $K = 6424$ i.i.d. points scatterers following a complex normal distribution:

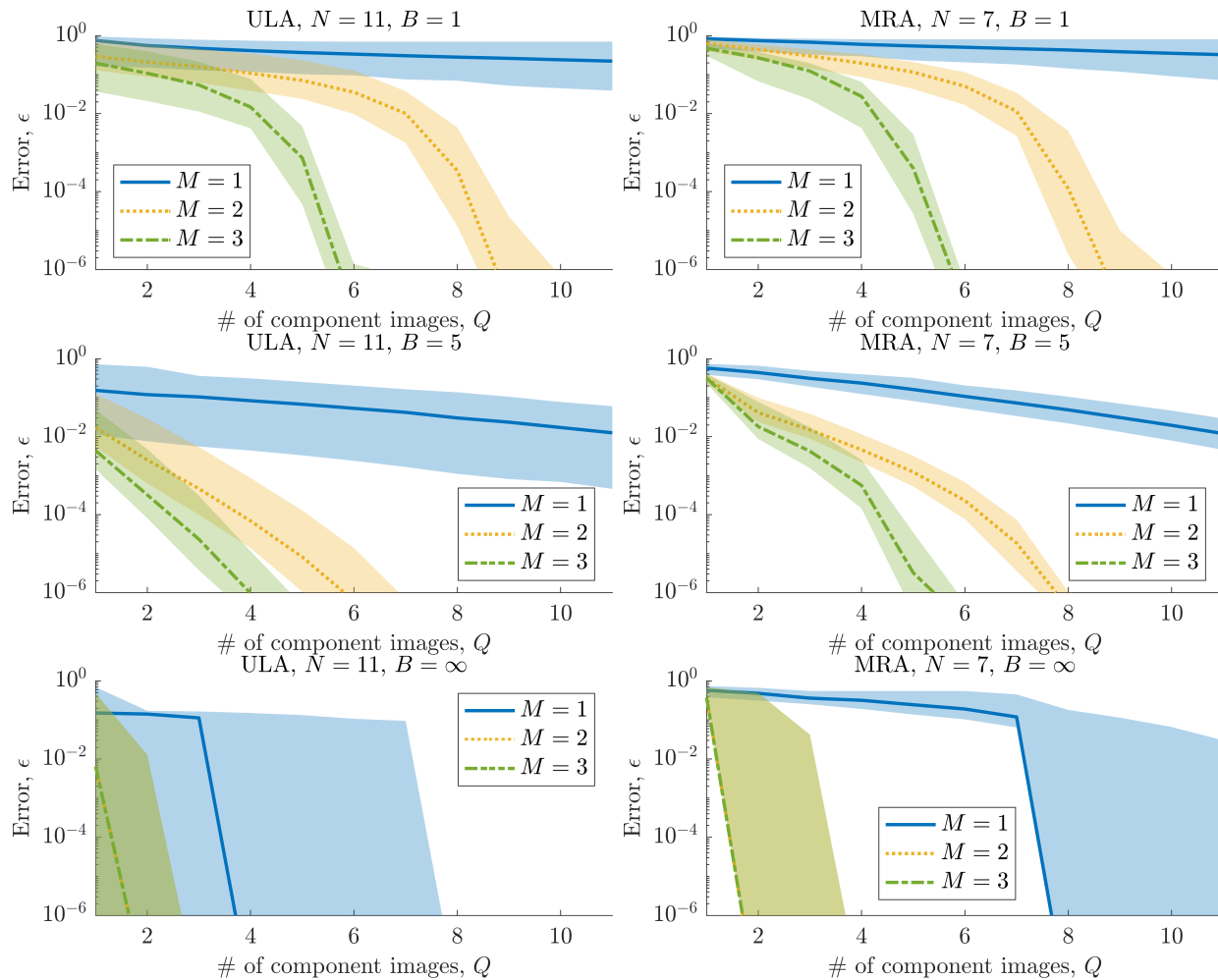


Fig. 12: Median error and 90% confidence intervals of hybrid ULA (left) and MRA (right) beamformers. Generally, the solution improves more by increasing M or Q , rather than B .

$\gamma_k \sim \mathcal{CN}(\frac{1}{\sqrt{2K}}, \frac{1}{2K})$. The variance of the measurement noise in (1) is $\sigma^2 = 1$. The desired (vectorized) two-dimensional co-array weighting is $\mathbf{w}_\Sigma = \mathbf{w}_{\text{DC}} \otimes \mathbf{w}_{\text{DC}}$, where $\mathbf{w}_{\text{DC}} \in \mathbb{R}^{17}$ is a one-dimensional Dolph-Chebyshev window with -40 dB sidelobes. We evaluate the PSF and image at $256 \times 256 = 65536$ pixels where the reduced azimuth and elevation angles $\sin(\varphi)$ and $\cos(\theta)$ are sampled uniformly at 256 points each in the interval $[-1, 1]$.

Fig. 14 (a) shows the noiseless PSF and the noisy image of the scattering scene produced by the fully digital URA. Algorithm 1 achieves the desired PSF using a single component image. In comparison, the fully digital BA in Fig. 14 (b) requires $Q = 6$ component images to attain the same PSF. By Theorem 1, the hybrid BA achieves exactly the same PSF as the fully digital BA, when $M = 2$, $B \rightarrow \infty$, and $Q = 6$. Remark 1 of Section IV also allows us to reduce

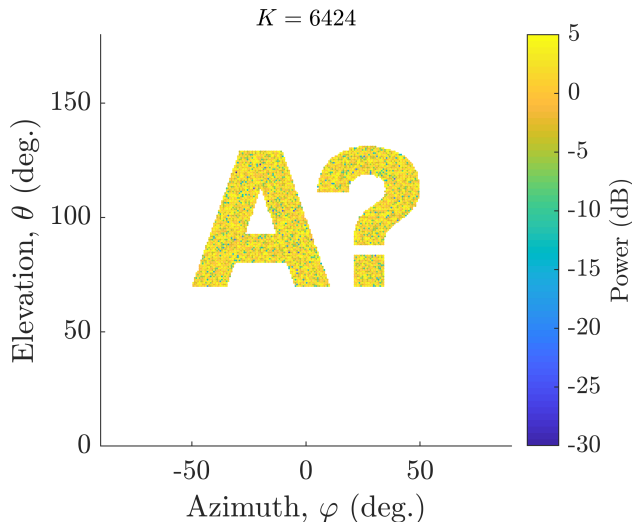


Fig. 13: Point scatterer distribution and normalized reflectivity.

the number of Tx/Rx front ends of the hybrid BA to $M = 1$, and still achieve the PSF of the fully digital BA using $Q = 6$ component images. Alternatively, we could reduce the number of phase shifters from 128 to 64 at the expense of increasing the number of component images to $Q = 4 \cdot 6 = 24$ (cf. Theorem 3).

Fig. 14 (c) shows the PSF and image produced by the hybrid BA using Algorithm 3 with $B = 5$ bit phase quantization, $M = 2$ Tx/Rx front ends, and $Q = 8$ component images. The phase quantization slightly degrades the PSF compared to Fig. 14 (b). However, the effect on the final image is not drastic. The main difference between the images produced by the BA (both fully digital and hybrid) and the URA is the lower noise level in the latter. Since the URA has more elements than the BA, it has at most $20 \log(289/64)^{\frac{3}{2}} \approx 20$ dB [33, Eq. (20)] higher array gain. However, the difference in the final SNR may be smaller than the difference in array gain, depending on the transmit power used in each component image.

Lastly, we note that the main computational effort in forming the discussed images stems from the number of times the beamforming weights need to be computed (see Section V-D). In the case of continuous phase shifters, solving (P1) once suffices, since the array may be steered in an arbitrary direction by applying appropriate phase shifts to its elements. This was the case in Fig. 14 (a) and (b), where a MATLAB [34] implementation of Algorithm 1 yielded a solution in a matter of seconds on a 2.3 GHz Intel Core i5 processor. In the case of Fig. 14 (c), the beamforming weights were recomputed for each pixel due to the quantized phase shifters. While

a single call of Algorithm 3 was on the order of a second, the complete image took 32 hours of processor time to compute (elapsed time was 20 hours). It is important to point out that, although it may be computationally intense, the beamforming weights can be computed offline and in parallel.

VIII. CONCLUSIONS

This paper considered active sensing using phased arrays with a hybrid beamforming architecture. The hybrid beamformers consist of a few Tx/Rx front ends, each connected to a network of inexpensive analog phase shifters with digitally controlled phase. Such hybrid beamformers have low cost and power consumption, which may be attractive in applications, such as, medical radar/ultrasound or automotive radar.

We formulated an optimization problem, where the transmit and receive hybrid beamforming weights are jointly found, such that a desired PSF is achieved using as few component images as possible. We proposed numerical methods for finding solutions in both the fully digital, as well as the hybrid and fully analog cases. Furthermore, we derived bounds on the maximum number of component images required by some of these hybrid and analog architectures for attaining the same PSF as their fully digital counterparts. Simulations demonstrated that combining sparse arrays with hybrid beamforming allows for significant reductions in the number of elements and front ends. In particular, we showed a design example, where a hybrid sparse planar array attained the PSF of a 17×17 element fully digital uniform square array using 78% fewer elements and 99% fewer Tx/Rx front ends. These hardware savings come at the price of an increase in the number of component images to 8 and a 20 dB reduction in array gain. However, multiple transmissions may simultaneously increase SNR. We observe that increasing the number of front ends or component images generally leads to higher fidelity PSFs than increasing the number of phase shift bits. Generally, only a few front ends are necessary for achieving the beamforming capabilities of a fully digital array. Indeed, two front ends are sufficient in the case of continuous phase shifters.

In future work, the proposed hybrid beamforming framework could be extended to the more general MIMO case, with several (possibly correlated) waveforms. It would also be of practical interest to explore constraints such as quantized ADCs/DACs or unit-modulus transmit beamforming weights.

APPENDIX A
PROOF OF LEMMA 1

Let $w_n \in \mathbb{C}$ be decomposed as

$$w_n = |c_1|e^{j(\angle c_1 + \phi_n)} + |c_2|e^{j(\angle c_2 + \vartheta_n)}, \quad (35)$$

where the phases $\phi_n, \vartheta_n \in [0, 2\pi)$ are functions of index $n = 1, 2, \dots, N$, but the complex amplitudes $c_1, c_2 \in \mathbb{C}$ are not. By the law of cosines, angles ϕ_n and ϑ_n can be written as

$$\begin{aligned} \phi_n &= \angle w_n - \angle c_1 + \cos^{-1} \left(\frac{|w_n|^2 + |c_1|^2 - |c_2|^2}{2|w_n||c_1|} \right) \\ \vartheta_n &= \angle w_n - \angle c_2 - \cos^{-1} \left(\frac{|w_n|^2 + |c_2|^2 - |c_1|^2}{2|w_n||c_2|} \right). \end{aligned}$$

Assume without loss of generality that $|c_1| \geq |c_2|$. It then follows from elementary trigonometry that (35) holds for all n only if c_1, c_2 satisfy conditions $|c_1| + |c_2| \geq \max_n(|w_n|)$, and $|c_1| - |c_2| \leq \min_n(|w_n|)$. For example, a particularly convenient choice is $c_1 = c_2 = \max_n |w_n|/2$, which leads to

$$\begin{aligned} \phi_n &= \angle w_n + \cos^{-1} \left(\frac{|w_n|}{\max_m |w_m|} \right) \\ \vartheta_n &= \angle w_n - \cos^{-1} \left(\frac{|w_n|}{\max_m |w_m|} \right). \end{aligned}$$

Using matrix notation then yields (13) and (14). □

APPENDIX B
PROOF OF LEMMA 2

We seek $\arg \min_{c \in \mathbb{C}, \mathbf{f} \in \mathcal{F}(\infty)} \|\mathbf{w} - \mathbf{c}\mathbf{f}\|_2^2$, or equivalently $\arg \min_{c \in \mathbb{C}, \boldsymbol{\phi} \in \mathbb{R}^N} J(c, \boldsymbol{\phi})$, where $f_n = e^{j\phi_n}$ and

$$\begin{aligned} J(c, \boldsymbol{\phi}) &= \sum_{n=1}^N \left| |w_n|e^{j\angle w_n} - |c|e^{j(\phi_n + \angle c)} \right|^2 \\ &= \sum_{n=1}^N |w_n|^2 + |c|^2 - 2|w_n||c| \cos(\phi_n + \angle c - \angle w_n). \end{aligned}$$

The minimizer is $\phi_n = \angle w_n - \angle c$, which yields $f_n = e^{j(\angle w_n - \angle c)}$. The least squares solution of c is then given by

$$c = (\mathbf{f}^H \mathbf{f})^{-1} \mathbf{f}^H \mathbf{w},$$

where $\mathbf{f}^H \mathbf{f} = N$ and $\mathbf{f}^H \mathbf{w} = \|\mathbf{w}\|_1 e^{j\angle c}$. Consequently, $|c| = \|\mathbf{w}\|_1 / N$, and

$$\begin{aligned} J\left(\frac{\|\mathbf{w}\|_1}{N} e^{j\angle c}, \angle \mathbf{w} - \angle c\right) &= \sum_{n=1}^N |w_n|^2 + \frac{\|\mathbf{w}\|_1^2}{N^2} - 2 \frac{|w_n| \|\mathbf{w}\|_1}{N} \\ &= \|\mathbf{w}\|_2^2 - \|\mathbf{w}\|_1^2 / N. \end{aligned}$$

Since $\angle c$ is a free parameter, we may select $\angle c = 0$ for simplicity, which yields (15) and (16). \square

APPENDIX C

PROOF OF LEMMA 3

Note that any $\mathbf{w} = \mathbf{F} \mathbf{c}$ can be written as $\mathbf{w} = \sum_{m=1}^M c_m \mathbf{F}_{:,m}$, where $\mathbf{F}_{:,m}$ is the m th column of matrix $\mathbf{F} \in \mathbb{C}^{N \times M}$, and $c_m \in \mathbb{C}$ is the m th element of vector $\mathbf{c} \in \mathbb{C}^M$. It follows that

$$\begin{aligned} \mathbf{W} &= \sum_{\tilde{q}=1}^Q \mathbf{w}_{r,\tilde{q}} \mathbf{w}_{t,\tilde{q}}^T \\ &= \sum_{\tilde{q}=1}^Q \left(\sum_{m_r=1}^{M_r} [\mathbf{c}_{r,\tilde{q}}]_{m_r} [\mathbf{F}_{r,\tilde{q}}]_{:,m_r} \right) \left(\sum_{m_t=1}^{M_t} [\mathbf{c}_{t,\tilde{q}}]_{m_t} [\mathbf{F}_{t,\tilde{q}}]_{:,m_t}^T \right) \\ &= \sum_{q=1}^{QM_r M_t} c_{r,q} c_{t,q} \mathbf{f}_{r,q} \mathbf{f}_{t,q}^T. \end{aligned}$$

A feasible choice relating indices \tilde{q} , m_r and m_t to index q is $\tilde{q} = \lceil q / (M_r M_t) \rceil$; $m_r = \lceil (1 + (q - 1) \bmod M_r M_t) / M_r \rceil$; and $m_t = 1 + (q - 1) \bmod M_t$. This then yields (28) and (29). \square

REFERENCES

- [1] H. L. Van Trees, *Optimum Array Processing, Part IV of Detection, Estimation, and Modulation Theory*. Wiley-Interscience, 2002.
- [2] R. T. Hoxor and S. A. Kassam, "The unifying role of the coarray in aperture synthesis for coherent and incoherent imaging," *Proceedings of the IEEE*, vol. 78, no. 4, pp. 735–752, Apr 1990.
- [3] P. Pal and P. P. Vaidyanathan, "Nested arrays: A novel approach to array processing with enhanced degrees of freedom," *IEEE Transactions on Signal Processing*, vol. 58, no. 8, pp. 4167–4181, Aug 2010.
- [4] M. Wang and A. Nehorai, "Coarrays, MUSIC, and the Cramér-Rao bound," *IEEE Transactions on Signal Processing*, vol. 65, no. 4, pp. 933–946, Feb 2017.
- [5] J. Li and P. Stoica, *MIMO radar signal processing*. John Wiley & Sons, 2009.
- [6] F. Ahmad, G. J. Frazer, S. A. Kassam, and M. G. Amin, "Design and implementation of near-field, wideband synthetic aperture beamformers," *IEEE Transactions on Aerospace and Electronic Systems*, vol. 40, no. 1, pp. 206–220, Jan 2004.
- [7] I. Ahmed, H. Khammari, A. Shahid, A. Musa, K. S. Kim, E. De Poorter, and I. Moerman, "A survey on hybrid beamforming techniques in 5G: Architecture and system model perspectives," *IEEE Communications Surveys Tutorials*, vol. 20, no. 4, pp. 3060–3097, 2018.

- [8] V. Venkateswaran and A. van der Veen, "Analog beamforming in MIMO communications with phase shift networks and online channel estimation," *IEEE Transactions on Signal Processing*, vol. 58, no. 8, pp. 4131–4143, Aug 2010.
- [9] A. Alkhateeb, J. Mo, N. González-Prelcic, and R. W. Heath, "MIMO precoding and combining solutions for millimeter-wave systems," *IEEE Communications Magazine*, vol. 52, no. 12, pp. 122–131, December 2014.
- [10] S. S. Ioushua and Y. C. Eldar, "A family of hybrid analog–digital beamforming methods for massive MIMO systems," *IEEE Transactions on Signal Processing*, vol. 67, no. 12, pp. 3243–3257, 2019.
- [11] A. F. Molisch, V. V. Ratnam, S. Han, Z. Li, S. L. H. Nguyen, L. Li, and K. Haneda, "Hybrid beamforming for massive MIMO: A survey," *IEEE Communications Magazine*, vol. 55, no. 9, pp. 134–141, September 2017.
- [12] X. Zhang, A. F. Molisch, and S.-Y. Kung, "Variable-phase-shift-based rf-baseband codesign for MIMO antenna selection," *IEEE Transactions on Signal Processing*, vol. 53, no. 11, pp. 4091–4103, Nov 2005.
- [13] E. Zhang and C. Huang, "On achieving optimal rate of digital precoder by rf-baseband codesign for MIMO systems," in *IEEE 80th Vehicular Technology Conference (VTC2014-Fall)*, Sept 2014, pp. 1–5.
- [14] F. Sotiraki and W. Yu, "Hybrid digital and analog beamforming design for large-scale antenna arrays," *IEEE Journal of Selected Topics in Signal Processing*, vol. 10, no. 3, pp. 501–513, April 2016.
- [15] T. E. Bogale, L. B. Le, A. Haghighat, and L. Vandendorpe, "On the number of rf chains and phase shifters, and scheduling design with hybrid analog–digital beamforming," *IEEE Transactions on Wireless Communications*, vol. 15, no. 5, pp. 3311–3326, May 2016.
- [16] X. Yu, J. Shen, J. Zhang, and K. B. Letaief, "Alternating minimization algorithms for hybrid precoding in millimeter wave MIMO systems," *IEEE Journal of Selected Topics in Signal Processing*, vol. 10, no. 3, pp. 485–500, April 2016.
- [17] J. Chen, "Hybrid beamforming with discrete phase shifters for millimeter-wave massive MIMO systems," *IEEE Transactions on Vehicular Technology*, vol. 66, no. 8, pp. 7604–7608, 2017.
- [18] J. Jin, Y. R. Zheng, W. Chen, and C. Xiao, "Hybrid precoding for millimeter wave MIMO systems: A matrix factorization approach," *IEEE Transactions on Wireless Communications*, vol. 17, no. 5, pp. 3327–3339, May 2018.
- [19] A. Arora, C. G. Tsinos, B. S. M. R. Rao, S. Chatzinotas, and B. Ottersten, "Hybrid transceivers design for large-scale antenna arrays using majorization-minimization algorithms," *IEEE Transactions on Signal Processing*, vol. 68, pp. 701–714, 2020.
- [20] A. Koochakzadeh and P. Pal, "Beam-pattern design for hybrid beamforming using wirtinger flow," in *IEEE 19th International Workshop on Signal Processing Advances in Wireless Communications (SPAWC)*, 2018, pp. 1–5.
- [21] O. E. Ayach, S. Rajagopal, S. Abu-Surra, Z. Pi, and R. W. Heath, "Spatially sparse precoding in millimeter wave MIMO systems," *IEEE Transactions on Wireless Communications*, vol. 13, no. 3, pp. 1499–1513, March 2014.
- [22] R. Rajamäki, S. P. Chepuri, and V. Koivunen, "Analog beamforming for active imaging using sparse arrays," in *53rd Asilomar Conference on Signals, Systems and Computers*, Asilomar, Pacific Grove, CA, November 2019, pp. 1202–1206.
- [23] R. J. Kozick and S. A. Kassam, "Linear imaging with sensor arrays on convex polygonal boundaries," *IEEE Transactions on Systems, Man, and Cybernetics*, vol. 21, no. 5, pp. 1155–1166, Sep 1991.
- [24] P. Jain, P. Netrapalli, and S. Sanghavi, "Low-rank matrix completion using alternating minimization," in *Proceedings of the forty-fifth annual ACM symposium on Theory of computing*. ACM, 2013, pp. 665–674.
- [25] G. H. Golub and C. F. Van Loan, *Matrix Computations 4th Edition*. The Johns Hopkins University Press, Baltimore, 2013.
- [26] A. Moffet, "Minimum-redundancy linear arrays," *IEEE Transactions on Antennas and Propagation*, vol. 16, no. 2, pp. 172–175, Mar 1968.
- [27] R. T. Hoctor and S. A. Kassam, "Array redundancy for active line arrays," *IEEE Transactions on Image Processing*, vol. 5, no. 7, pp. 1179–1183, Jul 1996.

- [28] J. Kohonen, “A meet-in-the-middle algorithm for finding extremal restricted additive 2-bases,” *Journal of Integer Sequences*, vol. 17, no. 6, 2014.
- [29] J. Kohonen, V. Koivunen, and R. Rajamäki, “Planar additive bases for rectangles,” *Journal of Integer Sequences*, vol. 21, no. 9, 2018.
- [30] R. Rajamäki and V. Koivunen, “Sparse active rectangular array with few closely spaced elements,” *IEEE Signal Processing Letters*, vol. 25, no. 12, pp. 1820–1824, Dec 2018.
- [31] P. Stoica and R. L. Moses, *Spectral analysis of signals*. Pearson Prentice Hall Upper Saddle River, NJ, 2005.
- [32] C. L. Dolph, “A current distribution for broadside arrays which optimizes the relationship between beam width and side-lobe level,” *Proceedings of the IRE*, vol. 34, no. 6, pp. 335–348, June 1946.
- [33] J. A. Johnson, M. Karaman, and B. T. Khuri-Yakub, “Coherent-array imaging using phased subarrays. part i: basic principles,” *IEEE Transactions on Ultrasonics, Ferroelectrics, and Frequency Control*, vol. 52, no. 1, pp. 37–50, Jan 2005.
- [34] MATLAB, *version 9.4.0.813654 (R2018a)*. Natick, Massachusetts: The MathWorks Inc., 2018.

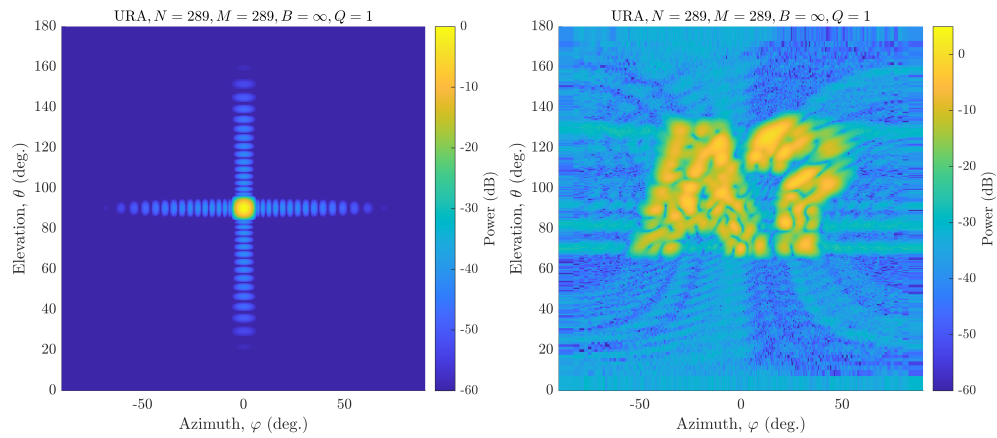
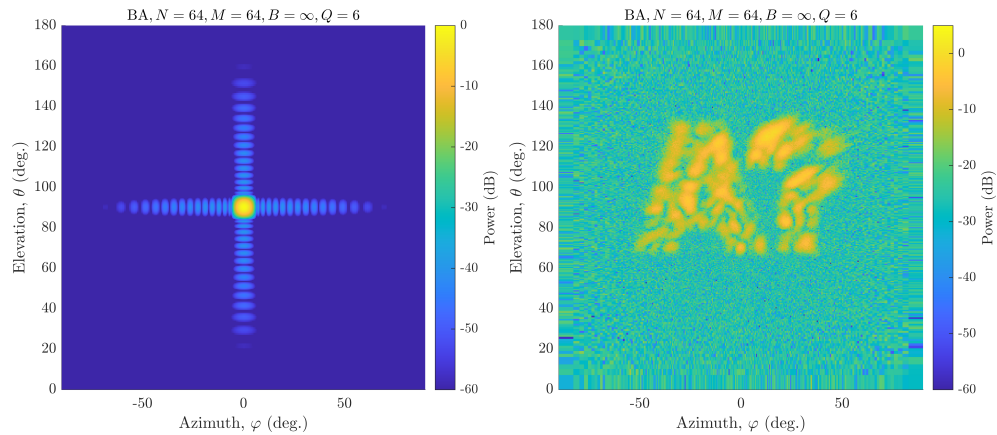
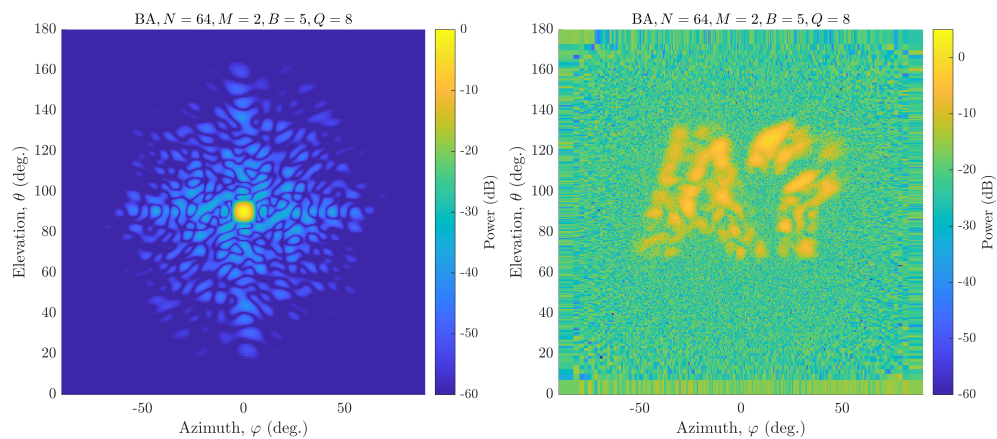
(a) Fully digital URA ($M = 289, Q = 1$)(b) Fully digital BA ($M = 64, Q = 6$)(c) Hybrid BA ($M = 2, Q = 8, B = 5$)

Fig. 14: PSF (left) and image of scatterer distribution (right). The hybrid BA attains a comparable image to the digital URA, at the expense of more component images and lower SNR.